



HAL
open science

Petrosal and bony labyrinth morphology of the stem paenungulate mammal (Paenungulatomorpha) *Ocepeia daouiensis* from the Paleocene of Morocco

Emmanuel Gheerbrant, Arnaud Schmitt, Guillaume Billet

► To cite this version:

Emmanuel Gheerbrant, Arnaud Schmitt, Guillaume Billet. Petrosal and bony labyrinth morphology of the stem paenungulate mammal (Paenungulatomorpha) *Ocepeia daouiensis* from the Paleocene of Morocco. *Journal of Anatomy*, inPress, 10.1111/joa.13255 . mnhn-02626224

HAL Id: mnhn-02626224

<https://mnhn.hal.science/mnhn-02626224>

Submitted on 25 Nov 2020

HAL is a multi-disciplinary open access archive for the deposit and dissemination of scientific research documents, whether they are published or not. The documents may come from teaching and research institutions in France or abroad, or from public or private research centers.

L'archive ouverte pluridisciplinaire **HAL**, est destinée au dépôt et à la diffusion de documents scientifiques de niveau recherche, publiés ou non, émanant des établissements d'enseignement et de recherche français ou étrangers, des laboratoires publics ou privés.

1 **Petrosal and bony labyrinth morphology of the stem paenungulate mammal**
2 **(Paenungulatomorpha) *Ocepeia daouiensis* from the Paleocene of Morocco**

3 Emmanuel Gheerbrant^{1*}, Arnaud Schmitt¹, and Guillaume Billet¹

4

5 ¹ *CR2P, Centre de Recherche en Paléontologie, Paris, UMR 7207 (CNRS, MNHN, UPMC,*

6 *Sorbonne Universités), Paris, France*

7 **corresponding author: emmanuel.gheerbrant@mnhn.fr*

8 **Abstract**

9 Based on high-resolution computed tomography, we describe in detail the petrosal and inner ear anatomy of one
10 of the few known African stem paenungulates (Paenungulatomorpha), *Ocepeia daouiensis* from the Selandian of the
11 Ouled Abdoun phosphate basin (Morocco). The petrosal of *Ocepeia* displays some remarkable, probably derived
12 features (among eutherians) such as relatively small pars cochlearis, pars canalicularis, and labyrinth (incl. small
13 semicircular canals), a large wing-like pars mastoidea, a large and inflated tegmen tympani, and the dorsoventral
14 orientation of the large canal for the ramus superior. The presence of small semicircular canals in *Ocepeia* is an
15 interesting shared trait with tenrecoidean afrotherians. Otherwise, and consistent with a general primitive skull
16 morphology, the middle ear and labyrinth of *Ocepeia daouiensis* is characterized by many plesiomorphic traits close
17 to the eutherian generalized plan. This adds to the rather generalized morphology of the earliest crown
18 paenungulates such as *Eritherium*, *Phosphatherium*, and *Seggeurius* to support an ancestral paenungulatomorph
19 morphotype poorly derived from the eutherian pattern. As a result, *Ocepeia* provides key morphological and fossil
20 data to test phylogenetic relationships of the Afrotheria (including Paenungulatomorpha) at the placental root mostly
21 inferred from molecular studies.

22 **Key words:** skull; petrosal; bony labyrinth; cochlea; computed tomography (CT); Paleocene;
23 Africa; *Ocepeia*; Paenungulata; Afrotheria.

24 **Introduction**

25
26 The condylarth-like mammal *Ocepeia daouiensis* from the Paleocene-Selandian (Yans et al.
27 2014; Kocsis et al. 2014) of the Ouled Abdoun Basin, Morocco, is the best known of the earliest
28 African placentals (Gheerbrant, 2010; Gheerbrant et al. 2014). Recently described material
29 includes the well-preserved skull MNHN.F.PM45. Its study by Gheerbrant et al. (2014)
30 supported that *Ocepeia daouiensis* is related to the Paenungulata as a stem taxon
31 (Paenungulatomorpha; see Fig. 1). The paenungulate stem relationship of *Ocepeia* was also
32 found in recent works of Gheerbrant et al. (2016, 2018) and Zack et al. (2019). *Ocepeia* is
33 actually the only known stem paenungulate together with *Abdounodus hamdii* (Gheerbrant et al.
34 2016).

35 The skull MNHN.F.PM45 preserves in particular the braincase and labyrinth endocasts. In
36 this work we describe and study in detail the petrosal morphology and the bony inner ear
37 morphology of *Ocepeia daouiensis* that was reconstructed as a 3D endocast model from a micro
38 CT scan of the skull MNHN.F.PM45. The reconstruction and study of the inner ear of *Ocepeia*
39 *daouiensis* were made based on both left and right petrosals preserved in specimen
40 MNHN.F.PM45 (Gheerbrant et al. 2014). The right and left semicircular canals are perfectly
41 aligned in profile in lateral view, showing that the petrosals are not distorted in MNHN.F.PM45.

42 The anatomy of the petrosal and inner ear of the afrotherians and its phylogenetic
43 significance were only recently investigated, and mostly based on the study of extant taxa
44 (Ekdale, 2013). However, several recent important fossil discoveries in the Paleogene of Africa
45 provided new key data on early afrotherians, including proboscideans (Schmitt & Gheerbrant,
46 2016), embrithopods (Benoit et al. 2013c), hyracoids (Benoit et al. 2015a) and macroscelideans
47 (Benoit et al. 2013b). *Ocepeia* adds to these fossil discoveries and provides the first direct
48 evidence on the ancestral petrosal and labyrinthine morphology of the Paenungulata.

49

50 **Material and Methods**

51

52 Collections, institutional abbreviations

53 OCP DEK/GE: Collections of the Office Chérifien des Phosphates, Khouribga, Morocco

54 MNHN.F: fossil collection of the Museum National d'Histoire Naturelle, France.

55 STIPB: Steinmann Institut Paläontologie Bonn.

56

57 Scan, modelisation, softwares

58 MNHN.F.PM45 was investigated by high-resolution computed tomography (μ CT) at the AST
59 – RX platform of the MNHN, Paris, using a GE Sensing and Inspection Technologies phoenix|x-
60 ray v|tome|x L240-180 CT scanner. We used the microfocus RX source 240kV/320W, detector
61 400 × 400 mm with a matrix of 2024 pixels (pixel size: 200x 200 μ m). Scan parameters:

62 Voltage=95 kV; Current=265 μ A; Isotropic voxel size of 0.02550441 mm. Data were
63 reconstructed using dat|x reconstruction software (Phoenix|x-ray, release 2.0) and then
64 exported into 16 bits TIFF images. We used the softwares MIMICS ($\text{\textcircled{R}}$ Materialise 2007,
65 Release 11.1) and Avizo 7.1.1 (Visualization Science Group) for the analysis, 3D modelisation,
66 visualisation and measurement of the tomographies. The 3D models of the petrosals and bony
67 labyrinths will be deposited and freely accessible on the Morphomuseum repository at
68 <https://morphomuseum.com/>.

69

70 Measurements (Fig. 2)

71 The volume of the petrosal was measured directly on the 3D model with MIMICS. Volumes of
72 the labyrinth were obtained using both the softwares MIMICS and Ariadne (David et al. 2016)
73 that computes volumes, lengths, areas and angles (see below). **The main goal of the Ariadne**
74 **software is to infer functional capacities of fossil taxa based on measurements of their bony**
75 **labyrinth, and through comparisons with the membranous ducts of relatively close taxa. In**
76 **addition, the Ariadne software can be used to simply provide several bony measurements (i.e.**
77 **semicircular central streamline length, cochlear length) that may be useful for further**
78 **comparisons and which are presented for *Ocepeia* in this paper.** The cochlear volume was
79 obtained by separating the cochlear part from the vestibular part using GEOMAGICS Studio
80 Studio 2012. The superior extremity of the cochlear canal as well as the fenestra vestibuli were
81 included in the cochlear part. On the other hand, the saccule was included in the vestibule part.

82 We measured with the software MIMICS the inner ear height (IEH) following Billet et al.
83 (2015) as the linear distance between the dorsal apex of the crus commune and the ventral apex
84 of the cochlea. The petrosal size index of *Ocepeia* was measured following Billet et al. (2015) as
85 the mean of the longest linear dimensions of the petrosal (excluding the mastoid part): the medial
86 length and anterior width of the tympanic face (PET L and PET W), and the cerebellar height
87 (PET H).

88 The **stapedial ratio** (Fig. 2A) was calculated following Segall (1970: L/W with $L =$
89 length and $w = \text{width}$ of the fenestra vestibuli). Calculation of the cochlear curvature follows
90 West (1985). The number of turns of the cochlea is measured following the protocol of West
91 (1985). The **aspect ratio** of the cochlea (Fig. 2B) was calculated according to the formula found
92 in Ekdale & Rowe (2011): H/W with $H = \text{height}$ and $W = \text{width}$ of the cochlea. Other linear
93 measurements of the labyrinth were obtained using the same custom software used for the
94 labyrinth volumes. The length of the cochlea was obtained through the sum of the distance of
95 consecutive landmarks and semilandmarks placed along the cochlea using AVIZO 7.1.1 (Fig.
96 2C-D) and calculated with the Ariadne software. The first anatomical landmark was located at
97 **the point of the external portion of the cochlea located in the continuation of the major axis of**
98 **the fenestra vestibuli.** The semilandmarks were then placed manually at approximately regular
99 distance along the external portion of the cochlea (which follows the basilar membrane) ($n \sim 50$).
100 The last anatomical landmark was placed at the tip of the helicotrema. For both the cochlea and
101 semicircular canals (see below), there was no sliding procedure for the semilandmarks as these
102 were only used in order to mark curves for non-linear measurements (e.g., cochlea length,
103 semicircular canal length).

104 Measurements of the semicircular canals were also landmark-based, but using central
105 streamlines of the canals calculated with the AutoSkeleton feature of AVIZO 7.1.1 (following
106 Gunz et al. 2012). **The central streamline is the line that follows the center of the bony canal over**
107 **its full length. It is obtained via the Autoskeleton functionality of the software Avizo. The**
108 **internal landmarks of the semicircular canals (lighter grey landmarks that are also represented**
109 **without the isosurface in Fig. 2C, D, E) are placed on this streamline. The central streamline**
110 **length of a semicircular canal is the sum of the distances between these landmarks (central**
111 **streamline landmarks) and the ampullar landmarks (the two very light grey landmarks on each**

112 canal, Fig. 2). The crus commune length consists of the sum of the distances between
 113 consecutive internal landmarks, and the semilandmarks were placed manually at approximately
 114 regular distance along the central streamline of the crus commune (from the intersection of the
 115 anterior and posterior canals streamline to the basis of the crus commune). The average section
 116 radius of the crus commune was given directly by the Ariadne software. It corresponds to the
 117 mean of the crus commune radii taken at different sections of the crus commune. We used these
 118 two values to calculate the **average thickness ratio** (average section radius / crus commune
 119 length * 100). This ratio gives a quantitative value that expresses the global thickness of the crus
 120 commune. Crus commune with a high ratio tend to be thicker and stockier than crus commune
 121 with a low ratio.

122 The semicircular canal length was calculated as the sum of the distances between
 123 consecutive landmarks and semilandmarks of the slender canal. For the anterior and posterior
 124 canals, the measurement starts at the center of the ampulla (at the level of the crista ampullaris)
 125 and ends at the level of the intersection of the two canals (first internal landmark of the crus
 126 commune). For the lateral canal, the measurement starts at the center of the ampulla and ends at
 127 the intersection with the lateral utricle. The average section radius was calculated in the same
 128 manner as for the crus commune average section radius. It expresses the mean section radius of
 129 the slender part of the canal. The average **thickness ratio** of each semicircular canal was
 130 calculated as the following formula: (average section radius / semicircular canal length) x 100.
 131 The mean of these three ratios expresses the **global thickness** of the semicircular canals
 132 quantitatively.

133 The angles between the semicircular canals were also given directly by the Ariadne
 134 software. Measuring manually these angles can be tricky because the semicircular canals are
 135 rarely perfectly planar. The software uses the landmarks to determine the functional plane of
 136 each semicircular canal (David et al. 2016). The angles were then compared between the
 137 functional planes of the canals.

138 Calculation of the **radii of curvature** of the semicircular canals uses the Spoor–Zonneveld
 139 equation (Spoor & Zonneveld, 1998): $R = ((L+W)/2) \times 0.5$, with L = length and W = width of the
 140 canals. Height and width of the semicircular canals were calculated from the center of the canal
 141 to the vestibule (which includes the ampullas) and following protocol of Macrini et al. (2010).

142 Figure 2 summarizes our measurement protocol of the bony labyrinth of *Ocepeia daouiensis*.

143

144 Comparisons

145 Anatomical comparisons were made with most early eutherians and placentals in which the
 146 petrosal and labyrinth are described based on the available CT observations: *Kulbeckia* (Ekdale,
 147 2013), zhelestids (Ekdale & Rowe, 2011; Ekdale, 2013), *Zalambdalestes* (Ekdale & Rowe,
 148 2011), *Protungulatum* (Orliac & O’Leary, 2016), *Carsiptychus* (Cameron et al. 2019), *Chriacus*
 149 (Bertrand et al. 2019), *Hyopsodus* (Ravel & Orliac, 2015), *Diacodexis* (Orliac et al. 2012),
 150 *Alcidedorbignya* (Muizon et al. 2015), *Leptictis* and *Leptictidium* (Ruf et al. 2016), *Notostylops*
 151 (Macrini et al. 2010, 2013), early diverging litopterns and notoungulates (Billet & Muizon, 2013;
 152 Billet et al. 2015), *Arsinoitherium* (Benoit et al. 2013c), *Prorastomus* (Benoit et al. 2013a), the
 153 undetermined sirenian from Chambi (Benoit et al. 2013a), *Chambius* (Benoit et al. 2013d),
 154 *Seggeurius* (Benoit et al. 2015a), *Eritherium* (Schmitt & Gheerbrant, 2016), *Phosphatherium*
 155 (Schmitt & Gheerbrant, 2016), *Numidotherium* (Benoit et al. 2013c; Court, 1992). Comparative
 156 anatomical data for extant placentals and especially afrotherians come from Benoit et al. (2015b)
 157 and Ekdale (2013). We used an anatomical terminology that generally follows the English
 158 equivalents of terms from the Nomina Anatomica Veterinaria, 5th edition (Waibl et al. 2005).
 159 When this practice was not appropriate (see Wible, 2010), terms were taken from the general
 160 comparative literature cited above.

161

162 Abbreviations

163 ASC: anterior semicircular canal, LSC: lateral semicircular canal, PSC: posterior semicircular
164 canal, SC: semicircular canal.

165
166 **The petrosal of *Ocepeia* (Figs 4-5)**

167
168 The basicranium of *Ocepeia daouiensis* preserves both right and left petrosals (see
169 Gheerbrant et al. 2014). While the petrosal is damaged in the mastoid region, the part containing
170 the inner ear is well preserved. Since there are no significant differences between the left and the
171 right ears, the measurements given below are an average of the left and right ear measurements,
172 except when mentioned otherwise.

173 The overall position and extension of the petrosal, as well as its general morphology within
174 the skull, are displayed in figure 3. [Figures 4-5](#) provide detailed views of the petrosal. The
175 petrosal index size measured following Billet et al. (2015) is 8.44 mm. The main features of the
176 middle ear were previously described by Gheerbrant et al. (2014) - only new observed
177 anatomical characters are described and compared below.

178 With respect to Gheerbrant et al. (2014), the comparisons are further developed with early
179 paenungulates such as the hyracoid *Seggeurius amourensis*, the proboscideans *Eritherium*
180 *azzouzorum* and *Phosphatherium escuillei*, and also the unnamed sirenian from Chambi (Benoit
181 et al. 2013a). *Ocepeia* shares a noticeable general resemblance with early paenungulates such as
182 *Seggeurius*, *Eritherium* and the unnamed sirenian from Chambi. It includes the shape and robust
183 construction of the *pars cochlearis* (Benoit et al. 2015a) and the inflated and barrel-like *tegmen*
184 *tympani*, although the latter is slightly more inflated in *Eritherium*. In rostral-ventral view, the
185 morphology of the petrosal of *Ocepeia* and *Eritherium* is strikingly similar. Both taxa share in
186 particular a large foramen in the *tegmen tympani* probably for the ramus superior of the stapedia
187 artery ([Fig. 4](#)). It suggests the presence of the stapedia artery in *Ocepeia*, as in *Seggeurius*. In
188 *Ocepeia*, the canal for the ramus superior is characterized by an original orientation from its
189 ventral opening within the *tegmen tympani*: it runs dorsally, and slightly laterally ([Fig. 5B](#)). In

190 *Eritherium*, it runs more anteriorly. *Ocepeia* is very similar to *Eritherium* in the morphology of
191 the stylomastoid notch that is delimited anterolaterally by a large bony ridge, the tympanohyal
192 (Fig. 4). This morphology, also seen in *Phosphatherium* (Gheerbrant et al. 2005, fig. 7), is likely
193 plesiomorphic for paenungulates. The promontorium is characterized by a very anterior position
194 in the petrosal, in association with a long and large mastoid apophysis in *Ocepeia* (Fig. 3A). The
195 promontorium shows a thick rostral tympanic process and a concave medial border representing
196 the sulcus of the inferior petrosal sinus (ips, Fig. 4). This sulcus is also well developed in
197 *Eritherium*. Medial to the sulcus of the inferior petrosal sinus, there is a flattened medial edge
198 that is reminiscent of a medial flange. The fenestra vestibuli of *Ocepeia* is elliptical. As in
199 *Eritherium*, the cochlear canaliculus (*aquaeductus cochleae*) opens ventro-medially in the
200 jugular fossa, more dorsally and more medially than the external aperture of the cochlear fossula
201 (which leads to the fenestra cochleae; see Wible et al. 2009, Billet and Muizon, 2013) (Fig. 4C).
202 The secondary facial foramen is visible on the right petrosal. It opens just laterally to the canal
203 for the ramus superior, well anterior to the fenestra vestibuli (Fig. 4B). It covers the cavum
204 supracochleare ventrally whose channel is directed somewhat more oblique than its posterior
205 prolongation, the facial sulcus. Anteriorly, the hiatus Fallopii is present as a small opening on the
206 anterior edge of the petrosal (Fig. 4A-B). Posterior to it, a large depressed area seems to be
207 present on the anterolateral portion of the promontorium, which could then correspond to the
208 tensor tympani fossa. However, this region has experienced some crushing and caution is thus
209 required for this identification. Posterior to the secondary facial foramen, the facial sulcus
210 borders the tympanic surface of the promontorium laterally. The facial sulcus is bordered
211 laterally by a low crista parotica (possibly damaged). The exact outline of the epitympanic recess
212 is unclear but it lies on the lateral aspect of the petrosal, dorsolaterally to the crista parotica and
213 posterior to the tegmen tympani. In its posterior part, the fossa incudis forms an oval-shaped
214 depression (Figs. 4B & 5A). There is no clear distinction of the stapedia fossa from the facial

215 sulcus posteriorly, showing that the former is not very well marked, except for a distinct
216 widening of the sulcus (Fig. 4C). In *Eritherium*, the stapedial fossa is not only wider but deeper
217 and thus more distinct from the facial sulcus. Ventromedial to the stapedial fossa, the external
218 aperture of the cochlear fossula is bordered posteriorly by a much reduced postpromontorial
219 tympanic sinus in *Ocepeia* (very thin anteroposteriorly and stretched mediolaterally). This space
220 is bordered posteriorly by a large and anteroposteriorly thick medial caudal tympanic process
221 that faces the entire external aperture of the cochlear fossula posteriorly (Fig. 4B). This appears
222 to be different from *Eritherium* in which the external aperture of the cochlear fossula is not
223 bordered by a postpromontorial sinus nor by a medial caudal tympanic process (*contra* Schmitt
224 & Gheerbrant, 2016), but is just opening directly ventromedially to the stapedial fossa. This thick
225 medial caudal tympanic process is present in *Seggeurius* where it is called “swelling on the
226 septum metacochleare” by Benoit et al. (2015a). A notch is present on the medial aspect of the
227 postpromontorial tympanic sinus of *Ocepeia*, between the medial caudal tympanic process and
228 the medial buttress of the external aperture of the cochlear fossula, possibly for the passage of
229 the tympanic nerve or for the auricular branch of the vagus nerve (see MacPhee, 1981; Evans &
230 de Lahunta, 2012; Billet et al. 2015; Muizon et al. 2015). In cerebellar view (Fig. 5C), the fossa
231 subarcuata of *Ocepeia* is deep as in *Eritherium*. However, the shape of the fossa differs between
232 the two taxa: in *Ocepeia*, the fossa has the shape of a lightly flattened cone while it is almost
233 spherical in *Eritherium*. The fossa subarcuata is much deeper in *Ocepeia* and *Eritherium* than in
234 *Phosphatherium*, and a little deeper than in *Seggeurius*. The internal auditory meatus and the
235 fossa subarcuata of *Ocepeia* are comparable in size, as in *Eritherium*. In *Seggeurius* and
236 *Phosphatherium* the area of the fossa subarcuata is by contrast larger than the internal auditory
237 meatus. The *foramen acusticum superius* and *inferius* of *Ocepeia* are separated by a distinct and
238 short *crista transversa*. It is as thick and short as in *Eritherium*, and thicker than in

239 *Phosphatherium* which displays a very narrow and long crista. The *crista transversa* is not
240 distinct in the cerebellar views of the petrosal of *Seggeurius* figured in Benoit et al. (2015).

241 On the dorsolateral (or squamosal) surface of the petrosal, a large sulcus is present in
242 continuation with the canal for the ramus superior of the stapedia artery. This sulcus runs in
243 posterodorsal direction on the dorsolateral edge of the petrosal (labelled stb? on Fig. 5D). On the
244 right petrosal, another sulcus seems to be present, and also runs towards the posterior direction,
245 dorsal to the base of the tegmen tympani (labelled pts? on Fig. 5A, D). This sulcus is not clearly
246 marked on the left petrosal, but the skull MNHN.F.PM45 is damaged in its left side, including
247 the left petrosal (whereas the right side and right petrosal are better preserved). The sulcus
248 running on the dorsolateral edge of the petrosal (stb? on Fig. 5D) likely represents a sulcus for a
249 posterior temporal ramus as it seems to connect with the large posterior temporal foramen in
250 *Ocepeia* (Gheerbrant et al. 2014: fig. 2). It may also have housed the capsuloparietal emissary
251 vein on its posterior portion (see Billet et al. 2015). The sulcus running directly dorsal to the
252 tegmen tympani (labelled “pts?” in Fig. 5) probably represents the posttemporal sulcus for the
253 diploëtica magna vessels (it could not be firmly confirmed from observations of the virtual slices
254 through the skull as the area that would correspond to the posttemporal canal is damaged,
255 especially posteriorly).

256 In *Eritherium*, a sulcus similar to those described in *Ocepeia* and running dorsally and then
257 posterodorsally on the dorsolateral edge of the squamosal surface of the petrosal is present, and
258 was recognized as a prootic sinus (Schmitt & Gheerbrant, 2016). The prootic canal is generally
259 absent in placentals, except in the extant *Solenodon* (Wible, 2008). Here the course of this sulcus
260 in *Eritherium* corresponds much better with the posttemporal canal and/or a sulcus for temporal
261 rami (Wible, 1993; Billet et al. 2015; Muizon et al. 2015), as found in *Ocepeia*. In addition, the
262 presence of a sulcus of the sigmoid sinus dorsomedial to the aforementioned sulcus (Schmitt &

263 Gheerbrant, 2016: fig. 2C) is erroneous in *Eritherium* and corresponds to a broken area partly
264 filled with cancellous bone.

265 The pars mastoidea is remarkably expanded, it is longer than the pars cochlearis and it
266 reaches the occipital face (Figs. 3, 5-6). The pars mastoidea forms a mediolaterally compressed
267 wing-like bony blade that is elongated and oblique anteroventral to posterodorsal (Fig. 3). The
268 posterior extent of the pars mastoidea is hard to determine accurately as the bony sutures in the
269 posteriormost part of the skull with the exoccipitals, parietal and squamosal are indistinct in a
270 damaged area of the skull. There is likely a small sliver of bone of the pars mastoidea posteriorly
271 exposed between the parietal and exoccipital (Fig. 3), that would thus participate to the external
272 occipital face (mastoid exposure condition), but its extent is not determinable. The pars
273 mastoidea of *Ocepeia daouiensis* is substantially pneumatized with numerous and large
274 trabeculae, especially in its dorsal part toward the supraoccipital which is itself also highly
275 pneumatized (Gheerbrant et al. 2014).

276 In conclusion, among paenungulates the petrosal of *Ocepeia* is more similar to that of
277 *Eritherium*. Resemblances are seen in the general proportions, and in several detailed features (a
278 deep fossa subarcuata which size is comparable to that of the internal auditory meatus, a very
279 inflated barrel-like *tegmen tympani*, a short crista transversa, the presence of a large foramen for
280 the ramus superior of the stapedia artery). As a whole, the middle ear of *Ocepeia* shows a
281 combination of (1) plesiomorphic eutherians traits such as the deep fossa subarcuata, the
282 promontorium weakly inflated and flanked by a flattened medial edge (associated to a thick
283 rostral tympanic process of uncertain evolutionary polarity), and a postero-medial external
284 aperture of the cochlear fossula (see Discussion), and (2) paenungulate features such as an
285 inflated and large *tegmen tympani*. The pierced *tegmen tympani* (foramen for the ramus superior
286 of the stapedia artery), known in several other eutherian groups, is also probably plesiomorphic
287 amongst placentals (Wible et al. 2001; Billet and Muizon, 2013; Muizon et al. 2015).

288

289 **The inner ear bony labyrinth**

290

291 Dimensions of the inner ear bony labyrinth

292 The total volume of the inner ear bony endocast of *Ocepeia daouiensis* is 17.53 mm³ and its inner
293 ear height (IEH; Billet et al. 2013) is 5.69 mm (Table 1). By comparison to the skull length and
294 body size of *O. daouiensis* (SL~ 90 mm, estimated body mass 3.5 kg; Gheerbrant et al. 2014),
295 this is a relatively small inner ear. Among afrotherians, *Procavia* has a relative labyrinth volume
296 to body mass and skull length noticeably greater than *Ocepeia* (*Procavia* specimen STIPB-
297 M6605: lab. vol.= 33.84 mm³, SL= 76 mm, BM= 3800 g.; BM in Nowak, 1999). Comparison of
298 the semicircular canals size (radius of curvature, SCR) relative to the body mass following the
299 method of Spoor et al. (2007) (see Fig. 8) also indicates that *Procavia* (taken from Benoit et al.
300 2015; see also similar values in Ekdale, 2013) has a larger inner ear, which is confirmed by its
301 higher IEH (IEH of specimen STIPB-M6605 = 8.16 mm, i.e. 143% of *Ocepeia*). We extended
302 the sample of the placental species studied by Spoor et al. (2007) with the addition of several
303 afrotherians for our comparison of the proportions of the labyrinth in *Ocepeia*. It shows that
304 *Ocepeia* shares a relative small size of the semicircular canals with several tenrecoid afrotherians
305 such as *Potamogale*, *Tenrec*, *Hemicentetes* and *Chrysochloris* (Fig. 8). By contrast other
306 afrotherians such as *Procavia* (hyracoid), *Orycteropus* (tubulidentate), *Macroscelides* and
307 *Rhynchocyon* (macroscelidids) have larger semicircular canals relative to their body mass.

308 The 3D reconstructed digital models display a relative small size of the inner ear of *Ocepeia*
309 *daouiensis* within the skull (Fig. 3). It also displays a relative small size of the bony labyrinth
310 within the petrosal (Figs. 3 and 6). This is well distinctive from the small-sized *Protungulatum*
311 where the bony labyrinth seems to occupy a large portion of the internal volume of the petrosal
312 (Orliac & O'Leary, 2016). In comparison, the relative small size of the inner ear of *Ocepeia*
313 *daouiensis* within the petrosal seems to be related to both its large and inflated tegmen tympani
314 and its very large wing-like mastoid portion. The ratio of the petrosal index size (PET size) to the

315 inner ear height (IEH) of *Ocepeia* (Table 1) indicates that the relative labyrinth and petrosal size
316 does not depart from the general proportions and growth trend seen in other measured placental
317 mammals (Billet et al. 2015). This is also true for *Eritherium* and *Phosphatherium* (Fig. 8 and
318 SI2). This suggests that this is actually the petrosal (pars cochlearis and pars canicularis), and
319 not only the labyrinth, that is small relative to the BM and skull length in *Ocepeia*. In this regard,
320 it is worth noting that the petrosal index size is based on linear measurements that do not include
321 the pars mastoidea which is large in *Ocepeia* especially relative to the pars cochlearis
322 (Gheerbrant et al. 2014: p. 7).

323
324 Cochlea (Figs. 6 - 7)

325 *Description and comparisons*

326 The cochlea of *Ocepeia daouiensis* is large with respect to the vestibule size. The volume ratio
327 of the cochlea with respect to the whole labyrinth is 66 %. This is similar to zhelestids (Ekdale &
328 Rowe, 2011; Orliac & O'Leary, 2016), and this is greater than in the reconstructed ancestral
329 morphotype of placentals and of afrotherians (Ekdale, 2013). The relative great proportion of the
330 cochlea in *Ocepeia* might be an eutherian plesiomorphic condition (Ekdale, 2013). The cochlea
331 length is 19.2 mm. By comparison, it is 16.05 mm in *Leptictidium* (Ruf et al. 2016) which has a
332 slightly larger IEH (6.44 mm) and a much smaller body size (BM: 466-627 g.). In the same way,
333 the *Leptictis* species studied by Ruf et al. (2016) has a close cochlear length (18.02 mm) and IEH
334 (5.3 mm), for a much smaller body size (BM: 400-1000 g) than *Ocepeia*. As noted above, it
335 confirms the small size of the bony labyrinth and petrosal (pars cochlearis and pars canicularis)
336 in *Ocepeia daouiensis*.

337 The number of coils of the cochlea measured following the method of West (1985) is 2.13
338 (765°). A cochlea with at least two turns is generally representative of the placental derived
339 condition by contrast to most Cretaceous eutherians that have only 1-1.5 turns (Meng & Fox,
340 1995; Ekdale & Rowe, 2011). However, some early diverging crown paenungulates such as

341 *Numidotherium* (540°-576°), *Prorastomus* (550°) and *Seggeurius* (688°), and also some
342 Paleocene placentals such as *Protungulatum* (553°), *Carsiptychus* (600°) and the pantodont
343 *Alcidedorbignya* (540°) have a less coiled cochlea, with less than two turns.

344 The ratio of the radius of the spiral base and spiral apex, also called grade of curvature of the
345 cochlea, is low: $R_{\text{base}}/R_{\text{apex}} = 2.75$. The spiral plane (lower coil) is oblique antero-dorsally, with an
346 angle of about 50-60° with respect to the plane of the LSC, depending of the angle of view. This
347 is significantly greater than in Cretaceous eutherian mammals; in zhelestids for instance, the
348 plane of the basal coil is tilted at 34° with respect to LSC plane (Ekdale & Rowe, 2011). The
349 pantodont *Alcidedorbignya* also has a smaller angle of the basal cochlear coil to LSC plane (35-
350 21°). The coiling is subplanar, as in the primitive eutherian condition: the basal coil is more or
351 less below the upper coil but the spiral coils do not separate fully from each other along the
352 coiling axis (Fig. 7C). The height to width aspect ratio of the cochlea cast is 0.72, close to the
353 values of *Carsiptychus*, *Hyopsodus* and the afrotherians *Moeritherium*, the undetermined
354 sirenian from Chambi and *Chambius*. In the coiling plan, the spiral coils are well separated from
355 each other (Fig. 7B) as in the zhelestids, *Carsiptychus*, *Hyopsodus* and *Alcidedorbignya*. This
356 character is uncommon amongst placentals. The spiral coils are in particular in contact (i.e.
357 coalescing) in basal paenungulates such as *Eritherium*, *Numidotherium*, *Prorastomus*, the
358 undetermined sirenian from Chambi (Benoit et al. 2013a), *Seggeurius* and *Arsinoitherium*. The
359 basal coil is enlarged in the area of the fenestra cochleae. The apical coil has a section diameter
360 comparable to the basal coil, and the helicotrema is large, but not inflated. This is distinctive
361 from *Notostylops*, but of uncertain polarity among eutherians. In ventral view there is a quite
362 distinct apical lacuna for the bony modiolus at the spiral apex.

363 The secondary bony spiral lamina extends on nearly all the basal coil (340-360° from f.
364 vestibuli; i.e. about 46% of cochlear can. length). This is comparable to some Cretaceous
365 eutherians such as zhelestids and zalambdalestids (Ekdale & Rowe, 2011), and to *Protungulatum*

366 and *Eritherium*. The secondary bony spiral lamina is a little shorter along the cochlear canal in
367 *Phosphatherium*, and more so in other crown placentals such as *Notostylops*, *Hyopsodus* and
368 *Diacodexis*. The width of the secondary bony spiral lamina within the cochlear canal is very
369 small (width from lateral wall of cochlear canal of about 0.1 mm). The secondary bony spiral
370 lamina is located high (dorsal) on the cochlear canal, indicating asymmetric development of the
371 scalae. The horizontal (XZ 740-760) and transverse (coronal) sections (XY 489) show indeed
372 that the scala vestibuli was larger than the scala tympani (see Gheerbrant et al. 2014, fig. 7). The
373 primary spiral bony lamina is well developed (width from axial wall of modiolus estimated as
374 0.3 mm); the distance from the primary basal spiral lamina to the lateral wall of the cochlea
375 (vestibular fissure), corresponding to the width of the basilar membrane (laminar gap), is about
376 0.3 mm (approximately same at base and apex). The modiolus appears in our CT scan sections of
377 the petrosal as a darker area indicating bone of typically lower density. The ganglion canals
378 (spiral canal) are poorly visible, but they seem distinct on some sections of the left petrosal (e.g.,
379 sections XZ 753, XY 491).

380 The fenestra vestibuli opens well below the lateral ampulla. It opens perpendicular with
381 respect to the external aperture of the cochlear fossula, as in *Seggeurius* (Benoit et al. 2015). It is
382 elliptical with a high stapedial ratio of 2.05. A high stapedial ratio value is also found in
383 *Protungulatum* (2.1) and Cretaceous eutherians such as *Kulbeckia* (2.0). The stapedial ratio is
384 lower in most paenungulates, even in the primitive genera such as *Eritherium* (1.57),
385 *Phosphatherium* (1.62), *Numidotherium* (1.8) and *Seggeurius* (1.79). A high stapedial ratio
386 might correspond to the primitive placental and eutherian condition (Segall, 1970; Macrini et al.
387 2010), but there is some variation amongst placentals (Ruf et al. 2016). For instance, a high
388 value of stapedial ratio is seen in some paenungulates such as the indeterminate sirenian from
389 Chambi (1.95) and the extant genera *Dendrohyrax* (2.5; Benoit et al. 2015) and *Procavia* (2.1).
390 Although smaller than the external aperture of the cochlear fossula, the fenestra vestibuli is

391 rather large, especially relative to paenungulates such as proboscideans (Table 1). This is the
 392 generalized condition and this is distinctive from *Phosphatherium* and *Numidotherium* (Schmitt
 393 & Gheerbrant, 2016). The external aperture of the cochlear fossula is large and postero-medially
 394 located with respect to the f. vestibuli. Its outline is noticeably elongated dorso-ventrally.

395 The cochlear canaliculus (perilymphatic duct) is well separated (distant) from the external
 396 aperture of the cochlear fossula, with an opening on the dorsal face of the cochlea. It is long and
 397 extends postero-dorso-medially. A posterior orientation of this canal is also observed in the
 398 zhelestids and in *Protungulatum*. The canal is large in diameter with respect to many placentals
 399 (e.g., *Notostylops*, *Protungulatum*), but similar to some marsupials (Schmelzle et al. 2007). Its
 400 cross-section is larger than that of the semicircular canals, and its opening enlarges nearly as the
 401 size of the external aperture of the cochlear fossula.

402 The aqueductus vestibuli (endolymphatic canal) is quite distinct. It originates from the
 403 vestibule just medial and anterior to the crus commune, as in zhelestids, *Alcidedorbignya* and
 404 *Protungulatum*. From the vestibule, it extends postero-dorsally, parallel to the crus commune to
 405 which it is closely appressed. Its base is bulged as in *Protungulatum*. It is very thin on most of its
 406 length, with a diameter much smaller than that of the semicircular canals.

407
 408 **Table 1:** Measurements of the cochlea and fenestrae of the bony labyrinth of *Ocepeia*
 409 *daouiensis* (mm)

Cochlea of <i>Ocepeia daouiensis</i>	
Volume of the labyrinth	17.5 mm ³
Volume of cochlea	11.65 mm ³
IEH Inner Ear Height	5.69 mm
PET size	8.44 mm
Number of coils	2.13 (765°)
Relative volume of the cochlea	66%
Length of cochlear canal	19.2 mm
Stapedial ratio	2.05
Ext. apert. coc. fossul. area	0.312 mm ³
Aspect ratio	0.72
Max Width of cochlea (diameter)	3.55 mm
Max Height of cochlea	2.1 mm

412

413

414 *Functional anatomy of the cochlea of Ocepeia daouiensis: Estimation of the frequency*
415 *range of hearing*

416
417 The cochlear size was shown to be related to the hearing sensitivity in mammals (e.g., West,
418 1985; Kirk & Gosselin-Ildari, 2009). We followed the predictive equations of West (1985) and
419 Meng & Fox (1995) to estimate the frequency range of the hearing in extant and fossil mammals
420 based on the dimensions of the cochlea. Our calculations based on these equations indicate that
421 the range of audible frequencies of *Ocepeia daouiensis* is between **29.5 and 0.12 kHz** at 60dB
422 sound pressure level (number of cochlear coils: 2.125; length of cochlea: 19.2 mm; see [Table 2](#)).
423 By comparison to the values recorded by Meng & Fox (1995: Fig. 6), *Ocepeia daouiensis* is
424 characterized by an intermediate sensitivity for low frequency sounds, between the lower limit of
425 extant placental mammals and the higher limit of Cretaceous therian mammals studied by Meng
426 & Fox (1995, Fig. 6). The low-frequency hearing limit of *Ocepeia* is also significantly lower
427 than that in *Protungulatum* (1.21 kHz in Orliac & O'Leary, 2016). *Ocepeia* consistently has a
428 longer basilar membrane (cochlear canal length) than in Cretaceous eutherians and
429 *Protungulatum*. In addition, the weak development in width of the secondary bony lamina in
430 *Ocepeia* agrees with a relative sensitivity for low frequency sounds. The low-frequency hearing
431 limit of *Ocepeia* calculated following Manoussaki et al. (2008) is 0.548 kHz (at 60 dB) which is
432 higher than value calculated following West (1985) and Meng & Fox (1995) and close to
433 *Diacodexis* (Orliac & O'Leary 2012). However, the reliability of the procedure of Manoussaki et
434 al. (2008) was questioned (e.g. Orliac & O'Leary 2016). *Ocepeia* also has lower value of the
435 upper-frequency limit with respect to those of the Cretaceous therians studied by Meng & Fox
436 (1995, Fig. 6).

437 We calculated the same hearing frequency range of *Ocepeia* using other published
438 equations by Rosowski & Graybeal (1991) and Rosowski (1992) based on basilar membranous
439 length (= length of cochlear canal): see [Table 2](#). The resulting hearing range of *Ocepeia* at 60 dB
440 was between 31.73 and 0.37 kHz. This is similar to the results calculated from West (1985)
441 method for the high-frequency limit, but higher for the low-frequency limit (at 60 dB SPL). It
442 should be however noted that the relevance of the prediction models of high frequency hearing in
443 mammals such as those of Rosowski (1992) have been recently questioned (e.g., Harper &
444 Rougier 2018).

445 The upper high frequency limit of *Ocepeia* was also estimated based on the interaural
446 distance (Hefner & Hefner, 2008; Ravel & Orliac, 2015). It provides a value ([Table 2](#)) in the
447 range of ultrasounds sensitivity (sound frequencies > 20 kHz, e.g. Ravel & Orliac, 2015),

448 although the restriction of the secondary bony lamina to the cochlea first turn indicates that
449 *Ocepeia* obviously was not specialised for high frequency hearing.

450

451 **Table 2:** Estimation of the hearing frequency range of *Ocepeia* based on its labyrinth
452 dimensions. LF: Low-frequency limit; HF: High-frequency limit. 1. Equation of West (1985),
453 Meng & Fox (1995), based on basilar membranous length (BML=cochlear canal length) and
454 number of coiling (N); Frequency limits at 60 dB Sound Pressure Level: $\log(\text{LF}) = 1.76 - 1.66$
455 $\log(\text{BML} \times \text{N})$; $\log(\text{HF}) = 2.42 - 0.994 \log(\text{BML}/\text{N})$. 2. Equation of Rosowski and Graybeal (1991)
456 and Rosowski (1992), based on basilar membraneous length (BML); frequency limits at 60 dB
457 Sound Pressure Level: $\log(\text{LF}) = 13(\text{BML}^{-1.2})$; $\log(\text{HF}) = 391(\text{BML}^{-0.85})$. 3. Equation of Hefner
458 & Hefner (2008): \log of high-frequency limit = $-0.4381 \times \log$ (functional interaural delay) +
459 2.7137 ; with functional interaural delay (microseconds) = interaural distance/0.3434 (see also
460 Ravel & Orliac 2015). 4. Equation of Manoussaki et al. (2008) for calculation of low-frequency
461 hearing limit based on the radii ratio (p) of the cochlea: $\text{LF} = 1.507 \exp.[-0.578(p-1)]$.

462

Equations bases	LF (kHz)	HF (kHz)	Comments
1 Basilar membranous length (BML=cochlear canal length) and number of coiling (N)	0.1219	29.4980	BML= 19.2 mm N= 2.125
2 Basilar membraneous length (BML)	0.3749	31.7227	BML= 19.2 mm
3 Interaural distance (ID) and delay	--	72.9805	ID= 30 mm
4 Radii ratio (p= Rbase/Rapex).	0.5481	--	p= 2.75

463

464 Vestibule of *Ocepeia daouiensis*

465 *Description and comparisons* (Fig. 7)

466 The semicircular canals of *Ocepeia daouiensis* are well developed, but with a low value of **1.42**
467 of the mean SCR (Table 3). Such low SCR value is usually found in small mammals, most
468 having a BM much lower than 1 kg (Spoor et al. 2007; Kemp & Kirk, 2014) (Fig. 8). It means
469 that the semicircular canals are relatively small in *Ocepeia daouiensis* relative to its body size.
470 The ratio of the mean radius (SCR) to the inner ear height (IEH) is 0.25, which supports that the
471 semicircular canals are not reduced relative to the inner ear size by comparison to other placental
472 mammals (e.g., most xenarthrans, litopterns; Billet et al. 2013, 2015).

473 The semicircular canals are noticeably thin with an average thickness ratio of 2.15. In
474 cross-section, the canals have a circular shape. All three semicircular canals display a slight
475 undulation. No ridges were observed on the semicircular canals.

476 The anterior semicircular canal (ASC) is the largest semicircular canal (Table 3), as most
477 usual in mammals (Cox & Jeffery, 2010) and eutherians (Ekdale & Rowe, 2011), but the
478 difference with the PSC is slight and it is seen mostly in height (=length of some authors). The
479 ASC shape is round. It is slightly curved caudally at the junction of the anterior ampulla. It does
480 not extend much more anteriorly than the anterior ampulla (subvertical connection). The central
481 streamline length of the ASC is 6.87 mm (Table 3) and its average section radius is 0.15 mm.
482 Therefore, the thickness ratio of this canal is 2.22 making it quite slender.

483 The lateral semicircular canal (LSC) is the smallest semicircular canal (Fig. 7). Its radius
484 of curvature is smaller than those of the anterior and posterior canals (Table 3). The angle of the
485 coiling axis (modiolus) and the LSC is 112.6°. The LSC shape is oval. The slender part of the
486 lateral semicircular canal is connected to the vestibule at a quite high position, above the PSC-
487 vestibule junction and the posterior ampulla. It is partly coalescent with the posterior ampulla
488 and thus forms a partial secondary crus commune. A complete secondary crus commune is
489 known in Cretaceous eutherians, as a plesiomorphic feature (Ekdale & Rowe, 2011). It is also
490 known in several placentals (e.g., Ekdale, 2013), including in afrotherians and paenungulates
491 such as the proboscidean *Phosphatherium* and *Numidotherium*, the sirenian from Chambi, and
492 the macroscelidean *Chambius* (Schmitt & Gheerbrant, 2016; Benoit et al. 2013a, 2013d). The
493 estimated length of the central streamline and the average section radius (0.14 mm) of the lateral
494 canal are similar to the other canals. The thickness ratio of the LSC is slightly lower (2.04) than
495 for the anterior and posterior canals. The LSC is curved dorsally in lateral view, as seen in
496 *Diacodexis* (Ravel & Orliac, 2015). In lateral view the LSC is ventrally canted of about 25° with
497 respect to the skull ventral base (basicranium, esp. basioccipital plane) and skull roof (e.g.,
498 sagittal crest) (Fig. 3). The same orientation is observed in the left and right labyrinths, which
499 indicates that it does not result from post-mortem distortion of the petrosals. It means that in
500 *Ocepeia daouiensis*, the head was significantly ventrally tilted when the LSC were horizontal
501 (Fig. 3D). A strongly nose-down head posture with horizontally held LSC is observed in several
502 other mammals such as armadillos (Coutier et al. 2017, Fig. 7) and *Plesiorcycteropus* (Benoit et
503 al. 2015b, Fig. 1). Coutier et al. (2017) showed that a high LSC–basicranium angle is also related
504 to some noticeable cranial characters such as strong nuchal crests for strong neck muscles in
505 some xenarthrans, which are indeed also seen in *Ocepeia*. A high LSC –basicranium angle has
506 also been proposed to be linked to a more ground-level based diet in some large mammals (e.g.,
507 rhinos in Schellhorn, 2018).

508 The posterior semicircular canal (PSC) is round (Fig. 7). It extends slightly more distally
509 than the LSC. It also extends in lower position with respect to the LSC (Fig. 7D) by contrast to

510 eutherians such as zhelestids, but much lower than in advanced paenungulates such as *Procavia*.
511 The posterior arc of the PSC is slightly curved ventrally. The central streamline length is similar
512 to the value found for the anterior canal although slightly longer (7.49 mm). The average section
513 radius is very similar to the anterior one (0.16 mm). Hence the thickness ratio of the posterior
514 canal (2.18) is very close to the ratio of the anterior canal (2.22). The radius of curvature of the
515 posterior canal is 1.25. The PSC does not extend significantly below the LSC.

516 The anterior and posterior semicircular canals meet high (at approximately 75% of the
517 height of the anterior canal). Hence, the crus commune of the ASC and PSC is elongated (longer
518 than the half height of the PSC), although less long than in generalized eutherians such as
519 zhelestids and *Zalambdalestes* (Ekdale & Rowe, 2011). In lateral view, with the LSC oriented
520 horizontal, the crus commune is noticeably inclined posteriorly as in zhelestid eutherians and in
521 *Protungulatum*; this is a likely plesiomorphic disposition for placentals. The crus commune in
522 *Ocepeia* has no marked basal thickening, and it is smooth without ridges. The average section
523 radius of the *crus commune* of *Ocepeia* is small (0.30 mm) and its length is approximately 1.75
524 mm. Therefore, *Ocepeia* has a *crus commune* with a relatively low thickness ratio (17.35).

525 The ampullae of *Ocepeia* are well-defined and inflated (Fig. 7). They are smooth and display
526 no ridges. The anterior ampulla is the most inflated and largest one. There is a distinct canal for
527 nervus ampullaris posterior (a branch of the vestibular nerve), that diverges from the posterior
528 ampulla and is directed anteriorly. It corresponds to the bony channel issued from the foramen
529 singulare.

530 The angles of semicircular canals in *Ocepeia* do not show strong deviation with respect to
531 the orthogonal orientation (Table 3), as in zhelestids. The greater deviation from the orthogonal
532 orientation is found in the angle between the ASC and LSC (Table 3). We calculated the angle
533 variance index from 90° of the three semicircular canals of *Ocepeia* following Malinzak et al.
534 (2012) and Ruf et al. (2016) as $\log_{90} \text{var} = 1, 57$.

535 On the vestibule, the spherical recess for the saccule and the elliptical recess for the
536 utricle form quite distinct but connected bulgings below the ASC (Fig. 7C). The condition of
537 *Ocepeia* is similar to *Chriacus*, *Protungulatum* and *Diacodexis* (Bertrand et al. 2019). According
538 to Bertrand et al. (2019) this morphology corresponds to “distinct, but not separated, chambers”
539 of utricle and saccule (their character 15-2). The position of the elliptical recess (and its
540 chamber) for the utricle is closer to the anterior end of the ASC than to its posterior end
541 (character 16-2 in Bertrand et al. 2019).

542 **Table 3a:** Dimensions of the semicircular canals of *Ocepeia daouiensis*

543

Angle ASC/PSC	91.6°
Angle ASC/LSC	80.1°
Angle PSC/LSC	87.8°
Length of crus commune	1.75 mm
Crus commune average section radius	0.30 mm
Crus commune average thickness ratio	17.4

544

545 **Table 3b:** Width (W) and height (H) of the semicircular canals of *Ocepeia daouiensis* (in mm;

546 measurement extending to mid canal section)

547

548

549

550

551

552

	ASC W	ASC H	PSC W	PSC H	LSC W	LSC H
Left labyrinth	3.26	3.01	3.05	2.77	2.38	2.63
Right labyrinth	3.12	3.06	3.05	2.83	2.41	2.61

553

554 **Table 3c:** Radius of curvature and other measurements of the semicircular canals of *Ocepeia*555 *daouiensis*. Radius of curvature calculated following the Spoor–Zonneveld equation (Spoor &556 Zonneveld, 1998): $R = ((H+W)/2) \times 0.5$, with H= height and W = width of the canals

557

	ASC	PSC	LSC	Mean
Radius of curvature (mean right and left labyrinths; mm)	1.52	1.50	1.25	1.42
Central streamline length (slender part; mm)	6.87	7.49	6.79	7.05
Average thickness ratio	2.22	2.18	2.04	2.15
Average cross-section diameter	0.15	0.16	0.14	0.15

559 *Functional characters of the semicircular canals of Ocepeia daouiensis*

560
 561 The value of the variance from orthogonality of the semicircular canals in *Ocepeia daouiensis*
 562 falls within the range shown by primates with medium head angular velocity magnitude (AVM).
 563 However, the poorly known intraspecific variation of the vestibular shape (e.g., Billet et al. 2012;
 564 Perier et al. 2016; Gonzales et al. 2019) raises questions on the functional interpretation of the
 565 angular variation of the semicircular canals in mammals (Ruf et al. 2016), and especially in fossil
 566 taxa. Benson et al. (2016) have also shown that the semicircular canals angles of birds strongly
 567 deviate from orthogonality and thus do not follow the trend suggested by Malinzak et al. (2012)
 568 for agile mammal taxa. Hence, the variation of the SC deviation from orthogonality certainly
 569 requires further study in extant mammals before stating on its potential functional meaning.

570
 571 **Table 4.** Body mass estimates of *Ocepeia daouiensis* in grams (*mean of upper and lower teeth;
 572 **estimation = minimal size). Predictive allometric equations from Damuth (1990),
 573 Damuth & MacFadden (1990) for all ungulates, selenodonts, and selenodont browsers.
 574 The best estimates (see Gheerbrant et al. 2014) are in bold (mean for all ungulates = 3.5
 575 kg; see text).
 576

Measurements base	All ungulates	Selenodont s	Selenodont browsers
Area M1*	9306,15	8769,99	7881,27
Area M2*	7556,50	7130,07	6358,69
Area M3*	5756,35	5188,77	4830,70
Length M1*	6924,72	6934,83	6357,63
Length M2*	4394,59	4037,88	3691,52
Length M3*	3484,46	2741,06	2687,64
Length M1-3*	4043,51	3846,18	3417,84
Skull length**	2950,34	--	--

577
 578
 579
 580 Spoor et al. (2007) have proposed a link between the agility of mammals and the size of
 581 their semicircular canals (radius of curvature, SCR) relative to their body mass. They designed
 582 predictive equations of agility categories (“agility score”) that could be used to infer the
 583 locomotory behaviour of extinct taxa (see also Silcox et al. 2009). However, criticism has been
 584 expressed on the subjectivity of the defined agility categories, on the weakness of the link
 585 between SCR and agility and on the simplistic view that one morphological parameter of the SC
 586 could suffice to predict agility (e.g., David et al. 2010, 2016; Malinzak et al. 2012). The
 587 significance of the “agility score” inferred from the semicircular canals size is indeed debated

588 and challenged (Graf & Klam, 2006; Kemp & Kirk, 2014; David et al. 2016; Benson et al. 2017;
589 Gonzales et al. 2019). In particular, Kemp & Kirk (2014) evidenced a more significant relation
590 of the variance of the semicircular canal size with those of the eye size and visual acuity. They
591 showed that once variance linked to body mass is removed, larger semicircular canals are found
592 in mammals with large eyes and higher visual acuity.

593 For these reasons, we do not discuss the significance for locomotion of the “agility
594 scores” calculated for *Ocepeia daouiensis* (Fig. 8). Instead, we plotted the mean radius of
595 curvature of the semicircular canals (SCR) and the body mass (BM in grams) in a graph
596 containing a wealth of mammalian species as previously studied and figured by Spoor et al.
597 (2007). The mean body mass of *Ocepeia daouiensis* was estimated as 3.5 kg (Table 4) based on
598 the length of M1-3, of M3 and of the skull (Gheerbrant et al. 2014). In the graph depicted in
599 figure 8, *Ocepeia* plots at very low SCR values, close to extant sloths. For the sake of
600 comparison, we added several extant afrotherians to the Spoor et al. (2007) dataset. It shows that
601 the insectivore-like afrotherians such as tenrecs and golden moles (tenrecoideans) share with
602 *Ocepeia* a small labyrinth with respect to other mammals with similar body mass. This shows
603 that both *Ocepeia* and some tenrecoideans share small semicircular canals relative to their body
604 mass, and in fact also small inner ears and petrosals (at least for *Ocepeia*, see above). It is
605 difficult to evaluate the size of the eyes in *Ocepeia*, but a gross estimate based on the
606 morphology and relative size of the orbit (Gheerbrant et al. 2014), as preserved in
607 MNHN.F.PM45, indicates rather small eyes relative to body mass (Kemp & Kirk, 2014, table 1),
608 with an estimated eye diameter around 15 mm. *Ocepeia* seems indeed to fit well with Kemp and
609 Kirk’s (2014) model that links relatively reduced semicircular canals and small eyes. The
610 distribution of the small eyes character state in afrotherians and its phylogenetic significance
611 remain to be investigated.

612

614 Discussion

615
616 One remarkable feature of *Ocepeia* is the small size of its petrosal (pars cochlearis and pars
617 canalicularis) and inner ear with respect to the skull and body size. The significance of a small
618 petrosal remains poorly known. However, and interestingly, we found that the semicircular
619 canals are also relatively small in tenrecoidean afrotherians which might be a shared
620 phylogenetic feature. A relatively small petrosal and labyrinth may be original and derived
621 within placentals, although more investigation is needed within this group. Its evolutionary state
622 within afrotherians remains uncertain (see below).

623 Our comparisons evidence the mostly plesiomorphic morphology of the petrosal of
624 *Ocepeia* among placentals, especially for the labyrinth; most noticeable symplesiomorphies are
625 reported in [Table 5](#). This is congruent with the skull morphology of *Ocepeia* (Gheerbrant et al.
626 2014) that resembles the stem eutherian pattern in many characters.

627 The ancestral morphotype of the bony labyrinth of the Afrotheria and Paenungulata was
628 previously characterized based on extant species (Ekdale, 2013). Recent important fossil
629 discoveries in the Paleogene of Africa provided new key data on the morphology of early
630 afrotherians, especially with the Selandian and Ypresian proboscideans *Eritherium* and
631 *Phosphatherium* (Schmitt & Gheerbrant, 2016), the early/middle Eocene hyracoid *Seggeurius*
632 (Benoit et al. 2015a), the unnamed early/middle Eocene sirenian from Chambi (Benoit et al.
633 2013a), the early/middle Eocene macroscelidean *Chambius* (Benoit et al. 2013b), and the
634 Oligocene embrithopod *Arsinoitherium* (Benoit et al. 2013c). The paenungulatomorph *Ocepeia*
635 (Gheerbrant et al. 2014) adds to these early taxa and further helps to enlighten the ancestral
636 labyrinthine morphology of the Paenungulata. It confirms several ancestral features inferred by
637 Ekdale (2013) ([Table 5](#): 1, 2, 7, 9) for the afrotherians. However, it also shows that the
638 afrotherian and paenungulatomorph labyrinth morphotypes were closer to the eutherian
639 morphotype in several characters listed in [Table 5](#). In particular, the relative cochlear volume
640 ([Table 5](#): 8) is greater in *Ocepeia* (66%) than in the ancestral morphotype reconstructed by
641 Ekdale (2013) for paenungulates (56%), afrotherians (56%) and placentals (58%). It is actually
642 close to the Afroinsectiphilia (64% in Ekdale, 2013), and to stem eutherians, which could
643 support it is a generalized feature of the Afrotheria. Another noticeable plesiomorphic trait
644 present in *Ocepeia* is the posteriorly inclined crus commune ([Table 5](#): 6).

645 With respect to eutherians and afrotherians, few specialized features are identified in
646 *Ocepeia*. The angle of the cochlea and LSC planes is larger in *Ocepeia* (60-50°) than in
647 zhelestids (29°-41°), but it remains still smaller with respect to most placentals. The aspect ratio

648 of the cochlea of *Ocepeia* (0.72) is higher than in non-placental eutherians, several early
649 placentals such as *Protungulatum* and *Alcidedorbignya*, and several paenungulates, including
650 early taxa such as *Eritherium* (0.35), *Numidotherium* (0.51), *Seggeurius* (0.48), and
651 *Arsinoitherium* (0.45). It is close or identical to *Chambius*, the sirenian from Chambi, and
652 *Moeritherium*, as a likely convergence. The incomplete separation of the posterior arm of the
653 LSC with the PSC is derived with respect to the true secondary crus commune known in
654 eutherians and also in afrotherians and paenungulates (e.g., *Phosphatherium*, *Numidotherium*,
655 the sirenian from Chambi, *Orycteropus* and *Chambius*). *Ocepeia* has an intermediate state of the
656 relative position of the PSC and LSC: the posterior arm of the PSC enters the vestibule in lower
657 position with respect to the LSC plane than in eutherians, but it is even lower in more derived
658 placental taxa such as *Procavia*. The cochlea of *Ocepeia* is slightly more coiled than in some
659 early paenungulates such as *Seggeurius* (688°) and *Numidotherium* (540 to 584°) and several
660 extant afrotherians (Ekdale, 2013). However, this character is subject to significant individual
661 variation (e.g., Schmitt 2016) which reduces its phylogenetic value. The large and inflated
662 tegmen tympani is derived with respect to stem eutherians and it is a remarkable shared trait with
663 paenungulates (Schmitt & Gheerbrant, 2016). However, this trait is known in other placentals. A
664 large and/or inflated tegmen tympani is known in some early euungulates (Ciffelli, 1982),
665 artiodactyls (O’Leary, 2010) and some South American extinct euungulates such as litopterns
666 and notoungulates (Billet et al 2015; Billet & Muizon 2013). It is unknown 1) if the state is
667 exactly homologous in these taxa, and 2) if this is a convergent trait of the Paenungulatomorpha
668 and other placentals. The distribution of this feature and its states among placentals actually need
669 to be further investigated. Similarly, the large and distally extended mastoid process is derived
670 with respect to eutherians. A large mastoid process is also known in proboscideans (Gheerbrant
671 et al. 2005), but the distribution of this feature within other Paenungulata remains poorly known.
672 A remarkable feature of *Ocepeia* is the dorsoventral orientation of the large canal for the ramus
673 superior. It may represent a derived feature, although here again it remains to be investigated in a
674 larger sample of extinct and extant placentals. The thick medial caudal tympanic process
675 described in *Ocepeia* is shared with *Seggeurius* in which it is called “a swelling on the septum
676 metacochleare” (Benoit et al. 2015a). The latter was interpreted as a possible synapomorphy of
677 the Sirenia and Hyracoidea (Benoit et al. 2015a). Its presence in *Ocepeia* argues for a more
678 generalized feature within paenungulatomorphs. Finally, the distinct but still connected
679 chambers of the utricle and saccule and the position of the utricle closer to anterior end of ASC
680 seen in *Ocepeia* correspond to two derived features within placentals according to Bertrand et al.
681 (2019; characters 15-2, 16-2). They suggested that these two traits support relationships of

682 *Chriacus* with crown euungulates such as the Artiodactyla. Nevertheless, *Ocepeia* demonstrates
683 a wider distribution of these features among placentals which are occurring at least in
684 paenungulatomorphs and euungulates.

685 The relatively small petrosal (pars cochlearis and pars canicularis) and its labyrinth might
686 be a basal afrotherian synapomorphy retained in tenrecoideans and in *Ocepeia*, and lost in crown
687 paenungulates and in other afroinsectiphilians. This hypothesis is favoured against the alternative
688 one of an exclusive synapomorphy of the tenrecoideans and *Ocepeia* because it is consistent with
689 the paenungulates relationships of *Ocepeia* (clade Paenungulatomorpha) supported by a large set
690 of other craniodental features (Gheerbrant et al. 2014, 2016, 2018). The distribution among
691 placentals of a relatively small labyrinth and petrosal as seen in *Ocepeia*, and its phylogenetic
692 significance remain, however, to be investigated in a cladistic analysis.

693 Several plesiomorphic traits of *Ocepeia* are also found in early crown paenungulates
694 (Table 5: 1, 2-5, 8-11, 15, 18). The petrosal and bony labyrinth of early crown paenungulates is
695 as a whole poorly specialized with respect to known stem paenungulates (paenungulatomorphs)
696 such as *Ocepeia*. This is especially true for the earliest known one, *Eritherium* (Schmitt &
697 Gheerbrant, 2016).

698

700 **Table 5.** Plesiomorphic features of *Ocepeia*, with indication of the putative ancestral
 701 morphotype taxonomic rank and primary reference inferring character polarity within mammals.
 702 References: (1) Billet et al. (2015), (2) Billet et Muizon (2013), (3) Coutier et al. (2017), (4) Ekdale
 703 (2013), (5) Ekdale & Rowe (2011), (6) Gheerbrant et al. (2014), (7) Macrini et al. (2007), (8) Macrini et
 704 al. (2010), (9) Macrini et al. (2013), (10) Meng & Fox (1995), (11) Muizon et al. (2015), (12) Orliac &
 705 O'Leary (2016), (13) Schmitt & Gheerbrant (2016).

706	707	708	709	710	711	712
#K	Structure	Character states seen in <i>Ocepeia</i>	Hypothetical ancestral morphotype	References		
1	Labyrinth	Largest SC: ASC	Theria, Eutheria	(1) (4) (9)		
2	Labyrinth	Thin semicircular canals	Theria, Eutheria	(1) (13)		
3	Labyrinth	High Crus Commune	Eutheria	(5)		
4	Labyrinth	Ampulla well inflated	Theria, Eutheria	(5)		
5	Labyrinth	Crus Commune posteriorly canted, far from anterior ampulla	Theria?, Eutheria	(12)		
6	Labyrinth	Cochlea with 2 turns (765°)	Placentalia convergences	(5) (10)		
7	Labyrinth	Cochlea vs labyrinth volume > 64 %	Theria, Eutheria	(4)		
8	Labyrinth	Closed angle of cochlea and LSC planes	Theria, Eutheria	(12)		
9	Labyrinth	Secondary bony lamina present, extended on all cochlea first turn	Theria, Eutheria, Placentalia?	(1)(10) (13)		
10	Labyrinth	High stapedial ratio (H>1.7)	Eutheria	(8)		
11	Labyrinth	Aq. vestibuli located antero-medial to the crus commune	Eutheria?, Placentalia	(12)		
12	Labyrinth	Aq. cochlearis posteriorly oriented	Eutheria?	(12)		
13	Labyrinth	Fen. vestibuli far ventrally from lateral ampulla	Eutheria?	(12)		
14	Labyrinth	Fen. vestibuli large (but smaller than external aperture of the cochlear fossula)	Eutheria	(13)		
15	Labyrinth	Spiral turns of cochlea loosely connected	Eutheria, Placentalia?	(11)		
16	Petrosal	Large and inflated tegmen tympani	Paenungulatomorpha? But also known in euungulates such as <i>Meniscotherium</i> , artiodactyls, litopterns, notoungulates (convergences?)	(6)		
17	Petrosal	tegmen tympani pierced by a large canal for the ramus superior	Eutheria, Placentalia?	(1) (2) (11)		
18	Petrosal	Deep and rounded fossa subarcuata	Theria, Eutheria	(1) (7) (13)		

714
715
716
717
718
719
720
721
722
723
724
725
726
727
728
729
730
731
732
733
734
735
736

Conclusion

The labyrinth morphology indicates that *Ocepeia* has a nose-down head posture when the LSC is held horizontally. The functional study of the cochlea evidences a higher sensitivity for low frequency sounds and a lower sensitivity for high frequency sounds of the hearing of *Ocepeia* with respect to Cretaceous eutherians. The petrosal of *Ocepeia* shows some remarkable traits such as its relatively small pars cochlearis, pars canicularis, and labyrinth (esp. SCs), a large wing-like pars mastoidea, a large and inflated tegmen tympani, and the dorsoventral orientation of the large canal for the ramus superior. The relative small size of the SCs and petrosal is shown to be an interesting shared trait with tenrecoidean afrotherians.

Ocepeia further shows that the ancestral morphotype of the petrosal and labyrinth in the Paenungulatomorpha retained many plesiomorphic features of the generalized eutherian pattern. This is in fact true for the whole skull morphology of *Ocepeia* (Gheerbrant et al. 2014). It is also consistent with the plesiomorphic morphology of the earliest known proboscidean *Eritherium* found in the same Selandian Ouled Abdoun phosphate beds (Gheerbrant, 2009; Schmitt & Gheerbrant, 2016). In this regard *Ocepeia* is among the very few available [fossils](#) documenting morphological features at the base of the Paenungulata and Afrotheria that should help to further test the relationships of the major clades diverging at the placental root, which are currently mostly based on molecular data (e.g., Madsen et al. 2001; Murphy et al. 2001; Springer et al. 2004; Foley et al. 2016). The formal phylogenetic significance of the labyrinthine features of early crown and stem paenungulates such as *Ocepeia* remains to be tested with a phylogenetic analysis.

737 **Acknowledgements**

738 We thank Romain David for discussion and use of the software Ariadne. We thank Miguel
739 Garcia Sanz (MNHN, AST-RX platform) for producing the CT scans and Florent Goussard and
740 Nathalie Poulet (CR2P) for assistance with 3D digital reconstructions and imaging based on CT
741 scans, and also for measurements on CT scan images and 3 D digital models. Silhouettes images
742 were downloaded from the PhyloPic website. We thank the three reviewers and the editor who
743 helped to improve our manuscript.
744

745 **References**

746

747 **Benoit J, Adnet S, El Mabrouk E, et al.** (2013a) Cranial Remain from Tunisia Provides
 748 New Clues for the Origin and Evolution of Sirenia (Mammalia, Afrotheria) in Africa.
 749 *PLoS ONE* 8(1): e54307. doi:10.1371/journal.pone.0054307.

750

Benoit J, Crumpton N, Merigeaud S, et al. (2013b) Petrosal and bony labyrinth
 751 morphology supports paraphyly of *Elephantulus* within Macroscelididae
 752 (Mammalia, Afrotheria). *J Mammal Evol* 21, 173-193. DOI:10.1007/s10914-
 753 013-9234-5.

754

Benoit J, Merigeaud S, Tabuce R (2013c) Homoplasy in the ear region of Tethytheria
 755 and the systematic position of Embrithopoda (Mammalia, Afrotheria). *Geobios* 46:
 756 357-370. <http://dx.doi.org/10.1016/j.geobios.2013.07.002>

757

Benoit J, Orliac M, Tabuce R (2013d) The petrosal of *Chambius* (Macroscelidea,
 758 Afrotheria) from the Eocene of Djebel Chambi (Tunisia) and the evolution of the ear
 759 region in elephant shrews. *J Syst Pal* 11, 907-923.
 760 DOI:10.1080/14772019.2012.713400.

761

Benoit, J, Crochet, J-Y, Mahboubi, M, et al (2015a) New material of *Seggeurius*
 762 *amourensis* (Paenungulata, Hyracoidea), including a partial skull with intact
 763 basicranium. *J Vert Pal* 36, e1034358. DOI:
 764 10.1080/02724634.2015.1034358.

765

Benoit J, Lehmann T, Vatter M, et al. (2015b) Comparative anatomy and three-
 766 dimensional geometric morphometric study of the bony labyrinth of
 767 Bibymalagasia (Mammalia, Afrotheria). *J Vert Pal* 35 (3), e930043.

768

Benson RBJ, Starmer-Jones E, Close RA, et al (2017) Comparative analysis of
 769 vestibular ecomorphology in birds. *J Anat* 231, 990 – 1018.

770

Bertrand OC, Shelley SL, Wible JR, et al (2019) Virtual endocranial and inner ear
 771 endocasts of the Paleocene ‘condylarth’ *Chriacus*: new insight into the neurosensory
 772 system and evolution of early placental mammals. *J Anat*,
 773 <https://doi.org/10.1111/joa.13084>.

774

Billet G, Muizon CD, (2013). External and internal anatomy of a petrosal from the late
 775 Paleocene of Itaboraí, Brazil, referred to Notoungulata (Placentalia). *J Vert Pal* 33,
 776 455–469. <https://doi.org/10.1080/02724634.2013.722153>

777

Billet G, Hautier L, Asher RJ, et al. (2012) High morphological variation of
 778 vestibular system accompanies slow and infrequent locomotion in three-toed
 779 sloths. *Proc R Soc B* 279, 3932–3939.

- 780 **Billet G, Germain D, Ruf I, et al.** (2013) Inner ear morphology in *Megatherium* and
781 insights on the evolution of vestibular system and locomotion in sloths. *J Anat*
782 223, 557–567.
- 783 **Billet G, de Muizon C, Schellhorn R, et al.** (2015) Petrosal and inner ear anatomy
784 and allometry amongst specimens referred to Litopterna (Placentalia). *Zool J*
785 *Linn Soc* 173, 956–987.
- 786 **Cameron J, Shelley S L, Williamson T E, et al.** (2019) The Brain and Inner Ear of
787 the Early Paleocene “Condylarth” *Carsiptychus coarctatus*: Implications for
788 Early Placental Mammal Neurosensory Biology and Behavior. *Anat Rec*
789 302(2), 306-324.
- 790 **Cifelli LR** (1982) The petrosal structure of *Hyopsodus* with respect to that of some other
791 ungulates, and its phylogenetic implications. *J Paleont* 56, 795–805.
- 792 **Court N** (1992) Cochlea anatomy of *Numidotherium koholense*: auditory acuity in
793 the oldest known proboscidean. *Lethaia* 25, 211-215.
- 794 **Coutier F, Hautier L, Cornette R, et al.** (2017) Orientation of the lateral semicircular
795 canal in Xenarthra and its links with head posture and phylogeny. *J Morph* 278 (5),
796 704–717.
- 797 **Cox PG, Jeffery N** (2010) Semicircular canals and agility: The influence of size
798 and shape measures *J Anat* 216, 37–47.
- 799 **Damuth J** (1990). Problems in estimating body masses of archaic ungulates using dental
800 measurements. In *Body size in mammalian paleobiology: estimation and biological*
801 *implications* (eds Damuth J, MacFadden BJ, pp 229–253. New York: Cambridge
802 University Press.
- 803 **Damuth J, MacFadden B J** (1990) *Body Size in Mammalian Paleobiology*. Cambridge:
804 Cambridge University Press.
- 805 **David R, Droulez J, Allain R, et al.** (2010). Motion from the past. A new method to infer
806 vestibular capacities of extinct species. *C R Palevol* 9, 397–410.
- 807 **David R, Stoessel A, Berthoz A, et al.** (2016) Assessing morphology and function of the
808 semicircular duct system: introducing new in-situ visualization and software toolbox.
809 *Sci Rep* 6, 32772.
- 810 **Ekdale EG** (2013) Comparative anatomy of the bony labyrinth (inner ear) of placental
811 mammals. *PLoS One* 8 (e66624), 1–100.
- 812 **Ekdale EG, Rowe T** (2011) Morphology and variation within the bony labyrinth of
813 zhelestids (Mammalia, Eutheria) and other therian mammals. *J Vert Pal* 31, 658-675.
- 814 **Evans H E, de Lahunta A** (2012). *Miller’s Anatomy of the Dog*. St Louis: Saunders.

- 815 **Foley N M, Springer M S, Teeling E C** (2016) Mammal madness: is the mammal tree of
 816 life not yet resolved? *Philosophical Transactions of the Royal Society B: Biological*
 817 *Sciences*, 371(1699), 20150140.
- 818 **Gheerbrant E, (2009)** Paleocene emergence of elephant relatives and the rapid radiation
 819 of African ungulates: *Proc Natl Acad Sci* 106, 10717–10721.
- 820 **Gheerbrant E** (2010). Primitive African ungulates ("Condylarthra" and Paenungulata). In
 821 *Cenozoic Mammals of Africa* (eds Werdelin L., Sanders W.J.), p. 563-571. Berkeley,
 822 Los Angeles, London: The University of California Press.
- 823 **Gheerbrant E, Sudre J, Tassy P, Amaghazaz M, Bouya B, Iarochene M, (2005).**
 824 Nouvelles données sur *Phosphatherium escuilliei* (Mammalia, Proboscidea) de
 825 l'Eocène inférieur du Maroc, apports à la phylogénie des Proboscidea et des ongulés
 826 lophodontes. *Geodiversitas* 27, 239–333.
- 827 **Gheerbrant E, Amaghazaz M, Bouya B, et al. (2014)** *Ocepeia* (middle Paleocene of
 828 Morocco): the oldest skull of an afrotherian mammal. *PLOS One* 9(2), 1-30 (DOI:
 829 10.1371/journal.pone.0089739).
- 830 **Gheerbrant E, Filippo A, Schmitt A** (2016) Convergence of Afrotherian and
 831 Laurasiatherian Ungulate-Like Mammals: First Morphological Evidence from the
 832 Paleocene of Morocco. *PLoS ONE* 11(7), 1-35. Doi:10.1371/journal.pone.0157556.
- 833 **Gheerbrant E, Schmitt A, Kocsis L** (2018) Early African Fossils Elucidate the Origin of
 834 Embriothopod Mammals. *Cur Biol* 28 (19), 2167-2173.
- 835 **Gonzales L A, Malinzak M D, Richard F K** (2019) Intraspecific variation in semicircular
 836 canal morphology—A missing element in adaptive scenarios? *Am J Phys Anthropol*,
 837 168, 10–24.
- 838 **Graf W, Klam F** (2006) Le système vestibulaire: anatomie fonctionnelle et comparée,
 839 évolution et développement. *C R Palevol* 5 (3–4): 637-655.
- 840 **Gunz P, Ramsier M, Kuhrig M, et al. (2012)** The mammalian bony labyrinth
 841 reconsidered, introducing a comprehensive geometric morphometric approach. *J Anat*
 842 6: 529–543.
- 843 **Harper T, Rougier G** (2018) Petrosal morphology and cochlear function in Mesozoic
 844 stem therians. bioRxiv preprint, online Dec. 7, 2018; doi:
 845 <http://dx.doi.org/10.1101/490367>
- 846 **Heffner RS, Heffner HE** (2008) *High-frequency hearing*. In *Handbook of the senses:*
 847 *audition* (eds Dallos P, Oertel D, Hoy R), p. 55–60. New York: Elsevier.
- 848 **Kemp AD, Kirk EC** (2014) Eye size and visual acuity influence vestibular anatomy in
 849 mammals. *Anat Rec* 297, 781–790.
- 850 **Kirk EC, Gosselin-Ildari AD** (2009) Cochlear labyrinth volume and hearing abilities in
 851 primates. *Anat Rec* 292, 765–776.
- 852 **Kocsis L, Gheerbrant E, Mouflih M, et al. (2014)** Comprehensive stable isotope
 853 investigation of marine biogenic apatite from the late Cretaceous—early Eocene
 854 phosphate series of Morocco. *Palaeogeogr, Palaeoclim, Palaeoecol* 394, 74–88.
- 855 **MacPhee RDE** (1981) Auditory regions of primates and eutherian insectivores.
 856 Morphology, ontogeny, and character analysis. *Contribution to Primatology* 18, 1, 1-
 857 284.

- 858 **Macrini TE, Rougier GW, Rowe T** (2007) Description of a cranial endocast from the
859 fossil mammal *Vincelestes neuquenianus* (Theriiformes) and its relevance to the
860 evolution of endocranial characters in therians. *Anat Rec* 290, 875–892.
861 (doi:10.1002/ar.20551)
- 862 **Macrini TE, Flynn JJ, Croft DA, et al.** (2010) Inner ear of a notoungulate placental
863 mammal: anatomical description and examination of potentially phylogenetically
864 informative characters. *J Anat* 216, 600–610.
- 865 **Macrini TE, Flynn J J, Ni X, et al.** (2013) Comparative study of notoungulate
866 (Placentalia, Mammalia) bony labyrinths and new phylogenetically informative inner
867 ear characters. *J Anat* 223(5), 442–461.
- 868 **Madsen O, Scally M, Douady CJ, et al.** (2001) Parallel adaptive radiations in two major
869 clades of placental mammals. *Nature* 409, 610–614.
- 870 **Malinzak MD, Kay RF, Hullar TE** (2012) Locomotor head movements and semicircular
871 canal morphology in primates. *Proc Natl Acad Sci USA* 109, 17914–17919.
- 872 **Manoussaki D, Chadwick RS, Ketten DR, et al** (2008) The influence of cochlear shape
873 on low-frequency hearing. *Proc Natl Acad Sci USA*, 105, 6162–6166.
- 874 **Meng J, Fox RC** (1995) Osseous inner ear structures and hearing in early marsupials and
875 placentals. *Zool J Lin Soc* 115, 47–71.
- 876 **Muizon C de, Billet G, Argot C, et al.** (2015) *Alcidedorbignya inopinata*, a basal
877 pantodont (Eutheria, Mammalia) from the early Palaeocene of Bolivia: anatomy,
878 phylogeny, and palaeobiology. *Geodiv* 37 (4), 397–634.
879 <https://doi.org/10.5252/g2015n4a1>
- 880 **Murphy W J, Eizirik W E, Johnson E, et al.** (2001) Molecular phylogenetics and the
881 origins of placental mammals. *Nature* 409: 614–618.
- 882 **Nowak R M** (1999) Walker's Mammals of the World. 6th Edition.
- 883 **O'Leary M A** (2010) An anatomical and phylogenetic study of the osteology of the
884 petrosal of extant and extinct artiodactylans (Mammalia) and relatives. *Bull Am Mus*
885 *Nat Hist* 335, 1–206
- 886 **Orliac M J, Benoit J, O'Leary M A** (2012) The inner ear of *Diacodexis*, the oldest
887 artiodactyl mammal. *J Anat* 221, 417–426
- 888 **Orliac M J, O'Leary M A** (2016) The inner ear of *Protungulatum* (Pan-Euungulata,
889 Mammalia). *J Mammal Evol* 23, 4, 337–352.
- 890 **Perier A, Lebrun R, Marivaux L** (2016) Different level of intraspecific variation of the
891 bony labyrinth morphology in slow-versus fast-moving primates. *J Mammal Evol* 23,
892 353–368.
- 893 **Ravel A, Orliac M** (2015) The inner ear morphology of the 'condylarthran' *Hyopsodus*
894 *lepidus*. *Hist Biol* 27, 957–969.
- 895 **Rosowski JJ** (1992) Hearing in transitional mammals: Predictions from the middle-ear
896 anatomy and hearing capabilities of extant mammals. In *The evolutionary biology of*
897 *hearing* (eds Webster DB, Fay RR, Popper AN), pp. 615–631. New York: Springer.
- 898 **Rosowski JJ, Graybeal A** (1991) What did *Morganucodon* hear? *Zool J Linn Soc* 101(2),
899 131–168. doi:10.1111/j.1096-3642.1991.tb00890.x

- 900 **Ruf I, Volpato V, Rose KD, et al.** (2016) Digital reconstruction of the inner ear of
901 *Leptictidium auderiense* (Leptictida, Mammalia) and North American leptictids
902 reveals new insight into leptictidan locomotor agility. *Paläontol Z* 90(1), 153–171.
903 doi:10.1007/s12542-015-0276-2.
- 904 **Schellhorn R** (2018) A potential link between lateral semicircular canal orientation, head
905 posture, and dietary habits in extant rhinos (Perissodactyla, Rhinocerotidae). *J Morph*
906 279 (1), 50 – 61.
- 907 **Schmitt A (2016)** La région de l'oreille osseuse chez les Proboscidea (Afrotheria,
908 Mammalia): anatomie, fonction, évolution, Doctoral dissertation, Paris, Muséum
909 national d'histoire naturelle.
- 910 **Schmitt A, Gheerbrant, E** (2016) The ear region of earliest known elephant relatives:
911 new light on the ancestral morphotype of proboscideans and afrotherians. *J Anat* 228,
912 137-152.
- 913 **Schmelzle T, Sánchez-Villagra MR, Maier W** (2007) Vestibular labyrinth diversity.
914 *Mammal Study* 32, 83-97.
- 915 **Segall W** (1970) Morphological parallelisms of the bulla and auditory ossicles in some
916 insectivores and marsupials. *Fieldiana Zool* 51, 169-205
- 917 **Silcox M.T, Bloch J.I, Boyer D.M, et al.** (2009). Semicircular canal system in early
918 primates. *J Hum Evol* 56, 315-327.
- 919 **Spoor F, Garland T, Krovitz G, et al.** (2007) The primate semicircular canal
920 system and locomotion. *Proc Natl Acad Sci USA* 104, 10808-10812.
- 921 **Spoor F, Zonneveld F** (1998) Comparative review of the human bony labyrinth. *Am J*
922 *Phys Anthropol* 107, 211-251.
- 923 **Springer MS, Stanhope MJ, Madsen O, et al.** (2004). Molecules consolidate the
924 placental mammal tree. *Trends Ecol Evol* 19, 430–438.
- 925 **Waibl H, Gasse H, Constantinescu GM, et al.** (2005) *Nomina Anatomica Veterinaria*.
926 5th ed. Hannover, Germany ; Columbia, MO, USA ; Ghent, Belgium: Editorial
927 Committee.
- 928 **West CD** (1985) The relationship of the spiral turns of the cochlea and the length of the
929 basilar-membrane to the range of audible frequencies in ground dwelling mammals. *J*
930 *Acoust Soc Am* 77, 1091-1101.
- 931 **Wible JR** (1993) Cranial circulation and relationships of the colugo *Cynocephalus*
932 (Dermoptera, Mammalia). *American Museum Novitates* 3072, 1-27.
- 933 **Wible JR** (2008) On the Cranial Osteology of the Hispaniolan Solenodon, *Solenodon*
934 *paradoxus* Brandt, 1833 (Mammalia, Lipotyphla, Solenodontidae). *Ann Carn Mus* 77,
935 321-402. doi:[10.2992/0097-4463-77.3.321](https://doi.org/10.2992/0097-4463-77.3.321).
- 936 **Wible JR** (2010) Petrosal anatomy of the nine-banded armadillo, *Dasypus novemcinctus*
937 Linnaeus, 1758 (Mammalia, Xenarthra, Dasypodidae). *Ann Carn Mus* 79, 1–29.
- 938 **Wible JR, Rougier GW, Novacek MJ, et al.** (2009) The Eutherian Mammal *Maelestes*
939 *gobiensis* from the Late Cretaceous of Mongolia and the phylogeny of cretaceous
940 eutheria. *Bulletin of the American Museum of Natural History* 2009, 1.
941 doi:[10.1206/623.1](https://doi.org/10.1206/623.1).

- 942 **Wible JR, Rougier GW, Novacek MJ, et al.** (2001) Earliest eutherian ear region: a
943 petrosal referred to *Prokennalestes* from the early Cretaceous of Mongolia. *Am Mus*
944 *Nov, New York*, **3322**, 1-44.
- 945 **Yans J, Amaghaz M, Bouya B, et al.** (2014) First carbon isotope chemostratigraphy of
946 the Ouled Abdoun phosphate Basin, Morocco; implications for dating and evolution of
947 earliest African placental mammals. *Gondwana Res* 25, 257–269.
- 948 **Zack SP, Rose KD, Holbrook LT, et al** 2019. An enigmatic new ungulate-like mammal
949 from the early Eocene of India. *Papers in Palaeontology* n/a.
950 <https://doi.org/10.1002/spp2.1288>
- 951
- 952

953 **Caption and list of figures**

954

955 **Fig. 1.** Simplified cladogram showing the phylogenetic relationships of *Ocepeia* within
956 Afrotheria (after Gheerbrant et al. 2014, 2016, 2018).

957 **Fig. 2.** Measurement protocol of the endocast of the inner ear of *Ocepeia daouiensis*.

958 (A) stapedial ratio (L = length, W = width); (B) cochlear aspect ratio (H = height, W =
959 width); (C) anterior semicircular canal central streamline length, (D) lateral semicircular
960 canal central streamline length; (E) posterior semicircular canal central streamline length;
961 (F) cochlear length; (G) length (ASCL) and width (ASCW) of the anterior semicircular
962 canal used to calculate the radius of curvature; (H) length (LSCL) and width (LSCW) of
963 the lateral semicircular canal used to calculate the radius of curvature.

964 **Fig. 3.** 3D digital model of the skull MNHN.F.PM45 of *Ocepeia daouiensis* showing by
965 transparency the petrosal and labyrinth, and the skull posture with the lateral semicircular
966 canal horizontally held (E, F, G).

967 (A-B), ventral views: A, modeling of the petrosals (yellow); B, modeling of the petrosals
968 (transparent, yellow) and labyrinths (red). (C-D), right lateral view with the lateral
969 semicircular canal (SCL) horizontally held: C, modeling of the petrosals (yellow); D,
970 modeling of the petrosals (transparent, yellow) and labyrinths (red). This figure displays
971 the relative small size of the inner ear in the petrosal of *Ocepeia daouiensis*, the large
972 extent of the mastoid part of the petrosal within the skull and the ventrally inclined posture
973 of the skull in C-D (SCL horizontal).

974 **Fig. 4.** 3D digital model of the petrosals of *Ocepeia daouiensis*, skull specimen MNHN.F.PM45.

975 (A), anterior view; (B), ventral view; (C), ventromedial view. Scale-bar: 4mm.

976 *Abbreviations:* aav, external aperture of the vestibular aqueduct; ab. X n.?, possible
977 notch/sulcus for the auricular branch of the vagus nerve (X); acan n, notch housing the
978 external aperture of the cochlear canaliculus; acf, external aperture of the cochlear fossula;
979 br., broken area; cp, crista parotica; fai, foramen acusticum inferius; fas, foramen
980 acusticum superius; fi, fossa incudis; fs, facial sulcus; fsa, fossa subarcuata; fv, fenestra
981 vestibuli; hf, hiatus Fallopii; iam, internal auditory meatus; ips, sulcus for the inferior
982 petrosal sinus; mctp, medial caudal tympanic process; mfe, medial flattened edge; mp,
983 mastoid part of the petrosal; pfc, prefacial commissure; pps, postpromontorial tympanic
984 sinus; pts?, possible posttemporal sulcus; rsup c, canal for the ramus superior (of the

985 stapedial artery); rtp, rostral tympanic process; sff, secondary facial foramen; smn,
 986 styломastoid notch; ttf, tensor tympani fossa; stf, stapedial fossa; stb?, possible sulcus for
 987 temporal branch; stf, stapedial fossa; thyl, tympanohyal; tt, tegmen tympani.

988 **Fig. 5.** 3D digital model of the petrosals of *Ocepeia daouiensis*, skull specimen MNHN.F.PM45.

989 (A), lateral view; (B), lateral view with transparency of the petrosal, and with the canal for
 990 the ramus superior of the stapedial artery highlighted; (C), cerebellar view; (D), dorsal
 991 view. Scale-bar: 4mm

992 *Abbreviations:* aav, external aperture of the vestibular aqueduct; ab. X n.?, possible
 993 notch/sulcus for the auricular branch of the vagus nerve (X); acan n, notch housing the
 994 external aperture of the cochlear canaliculus; acf, external aperture of the cochlear fossula;
 995 br., broken area; cp, crista parotica; er, epitympanic recess; fai, foramen acusticum
 996 inferius; fas, foramen acusticum superius; fi, fossa incudis; fs, facial sulcus; fsa, fossa
 997 subarcuata; fv, fenestra vestibuli; hf, hiatus Fallopii; iam, internal auditory meatus; ips,
 998 sulcus for the inferior petrosal sinus; mctp, medial caudal tympanic process; mfe, medial
 999 flattened edge; mp, mastoid part of the petrosal; pfc, prefacial commissure; pps,
 1000 postpromontorial tympanic sinus; pts?, possible posttemporal sulcus; rsup c, canal for the
 1001 ramus superior (of the stapedial artery); rtp, rostral tympanic process; sff, secondary facial
 1002 foramen; stb?, possible sulcus for temporal branch; stf, stapedial fossa; ttf, tensor tympani
 1003 fossa; thyl, tympanohyal; tt, tegmen tympani.

1004 **Fig. 6.** 3D digital model of the petrosals of *Ocepeia daouiensis*, specimen MNHN.F.PM45, with
 1005 the labyrinth by transparency.

1006 (A), right petrosal in cerebellar view; (B), left petrosal in cerebellar view; (C), right
 1007 petrosal in anterior view; (D), left petrosal in anterior view; (E), right petrosal in tympanic
 1008 view; (F), left petrosal in tympanic view. In red the labyrinth, in green the canal for the
 1009 ramus superior (of the stapedial artery) within the tegmen tympani. Scale-bar: 4mm

1010 **Fig. 7.** 3D reconstructed digital model of the left bony labyrinth of *Ocepeia daouiensis*, specimen
 1011 MNHN.F.PM45.

1012 (A) dorsal view, (B) anterior view, (C) medial view, (D) ventral view and (E) medio-
 1013 anterior view.

1014 *Abbreviations:* **aa** anterior ampulla, **asc** anterior semicircular canal, **av** aquaeductus
 1015 vestibuli, **cc** crus commune, **cca** cochlear canaliculus, **co** cochlea, **er** elliptical recess, **fc**

1016 *fenestra cochleae*, **fv** *fenestra vestibuli*, **la** lateral ampulla, **lsc** lateral semicircular canal, **pa**
1017 posterior ampulla, **psc** posterior semicircular canal, **sbl**, secondary bony lamina, **sr**,
1018 spherical recess, **va**, vestibular aqueduct. Orientation axes: dors dorsal; md medial, lat
1019 lateral, post posterior.

1020 **Fig. 8.** Graphical relationship between the size of the semicircular canals (SCR, radius of
1021 curvature) versus body-mass (BM), with the indication of agility estimates in various
1022 mammals as measured and compiled by Spoor et al. (2007). Measurements for *Ocepeia*
1023 *daouiensis*, and several extant afrotherians such *Orycteropus*, *Macroscelides*,
1024 *Rhynchocyon*, *Procavia*, *Dendrohyrax*, *Potamogale*, *Tenrec*, *Tenrec*, *Chrysochloris*,
1025 *Hemicentetes* were added to the dataset (silhouettes from PhyloPic website) (see SuppData
1026 S3). This diagram shows that *Ocepeia* and the insectivore-like afrotherians (Tenrecoidea)
1027 are characterized by a relative small size of the semicircular canals with respect to other
1028 mammals of the same body mass.

1029

1030 **Caption of Tables**

1031 **Table 1.** Measurements of the cochlea and fenestrae of the bony labyrinth of *Ocepeia daouiensis*
1032 (mm)

1033 **Table 2.** Estimation of the hearing frequency range of *Ocepeia* based on its labyrinth
1034 dimensions. LF: Low-frequency limit; HF: High-frequency limit. 1. Equation of West (1985),
1035 Meng & Fox (1995), based on basilar membranous length (BML=cochlear canal length) and
1036 number of coiling (N); Frequency limits at 60 dB Sound Pressure Level: $\log(\text{LF}) = 1.76 - 1.66$
1037 $\log(\text{BML} \times \text{N})$; $\log(\text{HF}) = 2.42 - 0.994 \log(\text{BML}/\text{N})$. 2. Equation of Rosowski and Graybeal (1991)
1038 and Rosowski (1992), based on basilar membraneous length (BML); frequency limits at 60 dB
1039 Sound Pressure Level: $\log(\text{LF}) = 13(\text{BML} - 1.2)$; $\log(\text{HF}) = 391(\text{BML} - 0.85)$. 3. Equation of
1040 Hefner & Hefner (2008): \log of high-frequency limit = $-0.4381 \times \log$ (functional interaural
1041 delay) + 2.7137; with functional interaural delay (microseconds) = interaural distance/0.3434
1042 (see also Ravel & Orliac, 2015). 4. Equation of Manoussaki et al. (2008) for calculation of low-
1043 frequency hearing limit based on the radii ratio (p) of the cochlea: $\text{LF} = 1.507 \exp.[-0.578(p-1)]$.
1044

1045 **Table 3a.** Dimensions of the semicircular canals of *Ocepeia daouiensis*.

1046 **Table 3b.** Width (W) and height (H) of the semicircular canals of *Ocepeia daouiensis* (in mm;
1047 measurement extending to mid canal section).

1048 **Table 3c.** Radius of curvature and other measurements of the semicircular canals of *Ocepeia*
1049 *daouiensis*. Radius of curvature calculated following the Spoor–Zonneveld equation (Spoor &
1050 Zonneveld, 1998): $R = ((H+W)/2) \times 0.5$, with H= height and W = width of the canals.

1051 **Table 4.** Body mass estimates of *Ocepeia daouiensis* (*mean of upper and lower teeth;
1052 **estimation = minimal size). Predictive allometric equations from Damuth (1990), Damuth &
1053 MacFadden (1990) for all ungulates, selenodonts, and selenodont browsers. The best (i.e., lower)
1054 estimates are in bold (mean for all ungulates = 3.5 kg; see text).

1055 **Table 5.** Plesiomorphic features of *Ocepeia*, with indication of the putative ancestral
1056 morphotype taxonomic rank and primary reference inferring character polarity within mammals.
1057 References: (1) Billet et al. (2015), (2) Billet et Muizon (2013), (3) Coutier et al. (2018), (4)
1058 Ekdale (2013), (5) Ekdale & Rowe (2011), (6) Gheerbrant et al. (2014), (7) Macrini et al. (2007),
1059 (8) Macrini et al. (2010), (9) Macrini et al. (2013), (10) Meng & Fox (1995), (11) Muizon et al.
1060 (2015), (12) Orliac & O'Leary (2016), (13) Schmitt & Gheerbrant (2016).

1061 **Supplementary information**

1062 **SI 1,** Video of the animated 3D CT scan model of the left labyrinth of *Ocepeia daouiensis* from
1063 the Paleocene of Morocco, specimen MNHN.F.PM45 (AVI file). Red: fenestra vestibuli; blue: f.
1064 cochleae; green: cochleae canaliculus.

1065 **SI2,** Data for the regression analysis between inner ear height and petrosal size.

1066 **SI3,** Data added (afrotherians) for the Figure 8, showing the graphical relationships of SCR, BM
1067 and agility categories.

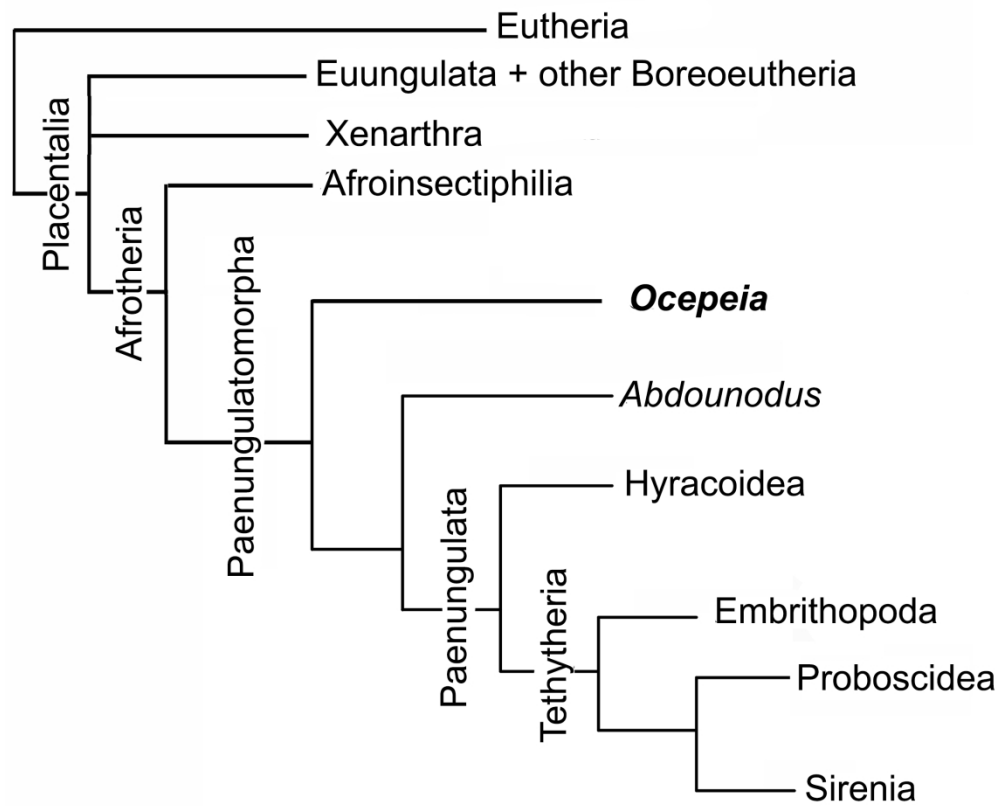


Fig. 1. Simplified cladogram showing the phylogenetic relationships of *Ocepeia* within Afrotheria (after Gheerbrant et al. 2014, 2016, 2018).

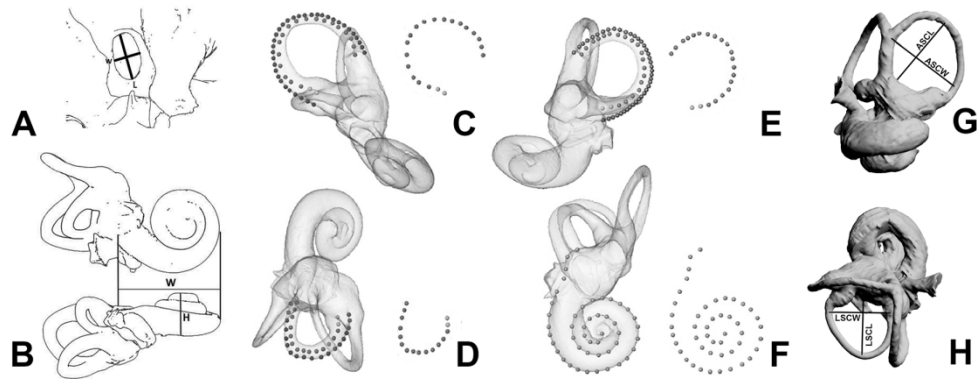


Fig. 2. Measurement protocol of the endocast of the inner ear of *Ocepeia daouiensis*. (A) stapedial ratio (L = length, W = width); (B) cochlear aspect ratio (H = height, W = width); (C) anterior semicircular canal central streamline length, (D) lateral semicircular canal central streamline length; (E) posterior semicircular canal central streamline length; (F) cochlear length; (G) length (ASCL) and width (ASCW) of the anterior semicircular canal used to calculate the radius of curvature; (H) length (LSCL) and width (LSCW) of the lateral semicircular canal used to calculate the radius of curvature.

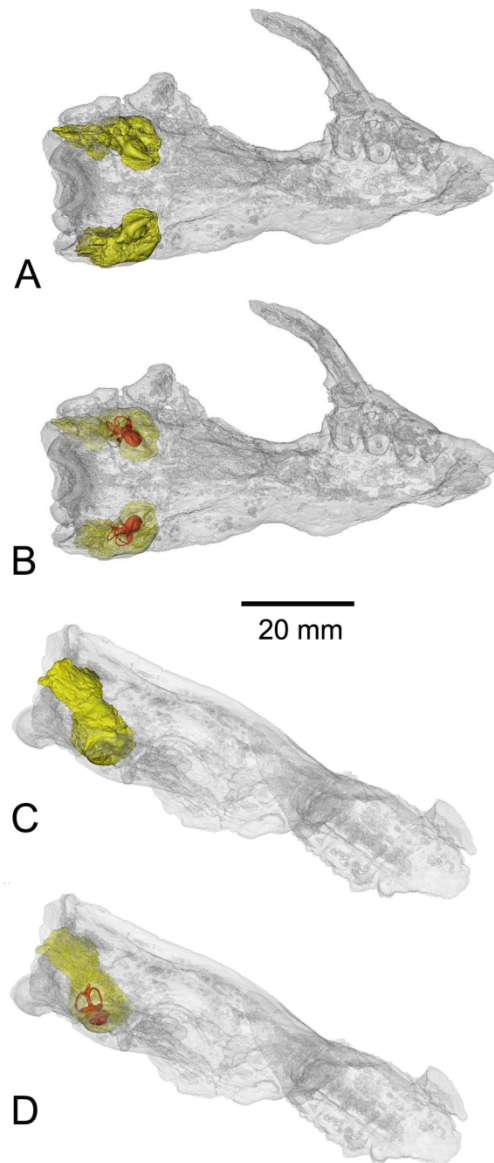


Fig. 3. 3D digital model of the skull MNHN.F.PM45 of *Ocepeia daouiensis* showing by transparency the petrosal and labyrinth, and the skull posture with the lateral semicircular canal horizontally held (E, F, G). (A-B), ventral views: A, modeling of the petrosals (yellow); B, modeling of the petrosals (transparent, yellow) and labyrinths (red). (C-D), right lateral view with the lateral semicircular canal (SCL) horizontally held: C, modeling of the petrosals (yellow); D, modeling of the petrosals (transparent, yellow) and labyrinths (red). This figure displays the relative small size of the inner ear in the petrosal of *Ocepeia daouiensis*, the large extent of the mastoid part of the petrosal within the skull and the ventrally inclined posture of the skull in C-D (SCL horizontal).

77x181mm (300 x 300 DPI)

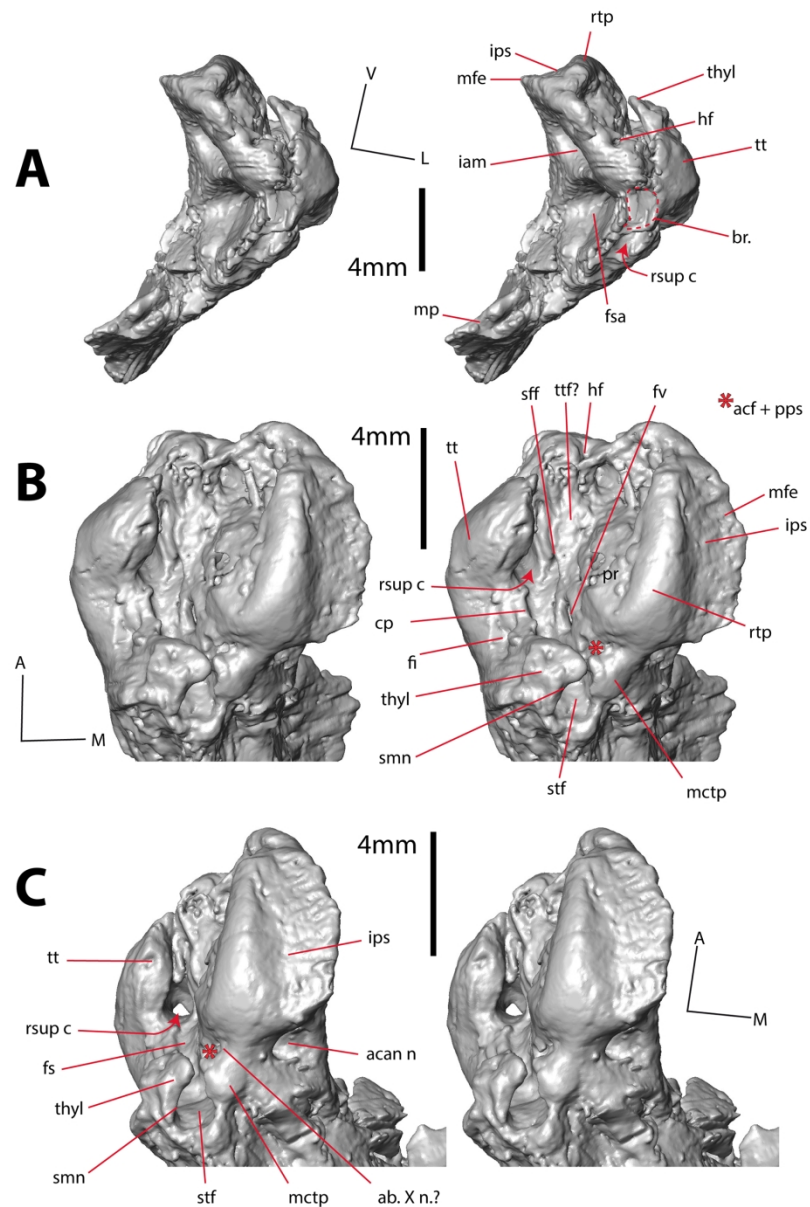


Fig. 4. 3D digital model of the petrosals of *Ocepeia daouiensis*, skull specimen MNHN.F.PM45. (A), anterior view; (B), ventral view; (C), ventromedial view. Scale-bar: 4mm.

Abbreviations: aav, external aperture of the vestibular aqueduct; ab. X n.?, possible notch/sulcus for the auricular branch of the vagus nerve (X); acan n, notch housing the external aperture of the cochlear canaliculus; acf, external aperture of the cochlear fossula; br., broken area; cp, crista parotica; fai, foramen acousticum inferius; fas, foramen acousticum superius; fi, fossa incudis; fs, facial sulcus; fsa, fossa subarcuata; fv, fenestra vestibuli; hf, hiatus Fallopii; iam, internal auditory meatus; ips, sulcus for the inferior petrosal sinus; mctp, medial caudal tympanic process; mfe, medial flattened edge; mp, mastoid part of the petrosal; pfc, prefacial commissure; pps, postpromontorial tympanic sinus; pts?, possible posttemporal sulcus; rsup c, canal for the ramus superior (of the stapedial artery); rtp, rostral tympanic process; sff, secondary facial foramen; smn, stylo-mastoid notch; ttf, tensor tympani fossa; stf, stapedial fossa; stb?, possible sulcus for temporal branch; stf, stapedial fossa; thyl, tympanohyal; tt, tegmen tympani.

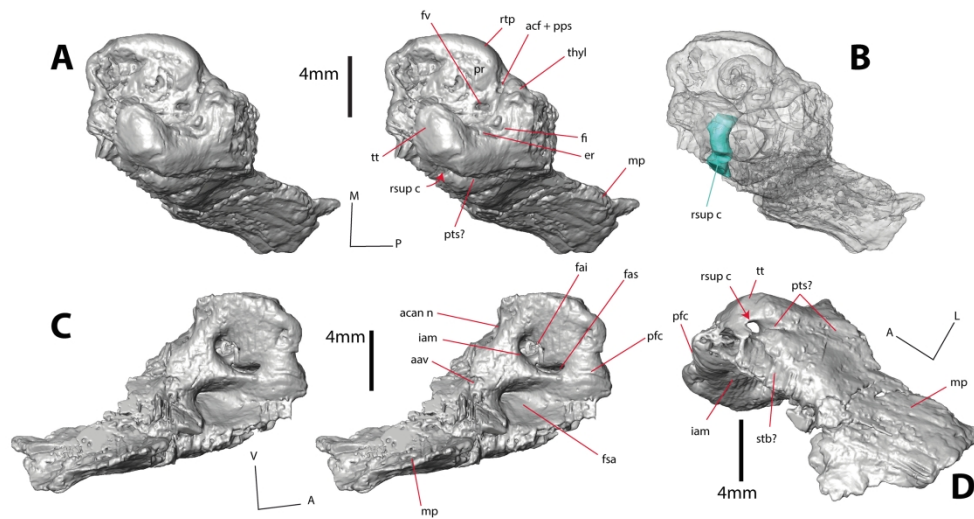


Fig. 5. 3D digital model of the petrosals of *Ocepeia daouiensis*, skull specimen MNHN.F.PM45. (A), lateral view; (B), lateral view with transparency of the petrosal, and with the canal for the ramus superior of the stapedial artery highlighted; (C), cerebellar view; (D), dorsal view. Scale-bar: 4mm
 Abbreviations: aav, external aperture of the vestibular aqueduct; ab. X n.?, possible notch/sulcus for the auricular branch of the vagus nerve (X); acan n, notch housing the external aperture of the cochlear canaliculus; acf, external aperture of the cochlear fossula; br., broken area; cp, crista parotica; er, epitympanic recess; fai, foramen acusticum inferius; fas, foramen acusticum superius; fi, fossa incudis; fs, facial sulcus; fsa, fossa subarcuata; fv, fenestra vestibuli; hf, hiatus Fallopii; iam, internal auditory meatus; ips, sulcus for the inferior petrosal sinus; mctp, medial caudal tympanic process; mfe, medial flattened edge; mp, mastoid part of the petrosal; pfc, prefacial commissure; pps, postpromontorial tympanic sinus; pts?, possible posttemporal sulcus; rsup c, canal for the ramus superior (of the stapedial artery); rtp, rostral tympanic process; sff, secondary facial foramen; stb?, possible sulcus for temporal branch; stf, stapedial fossa; ttf, tensor tympani fossa; thyl, tympanohyal; tt, tegmen tympani.

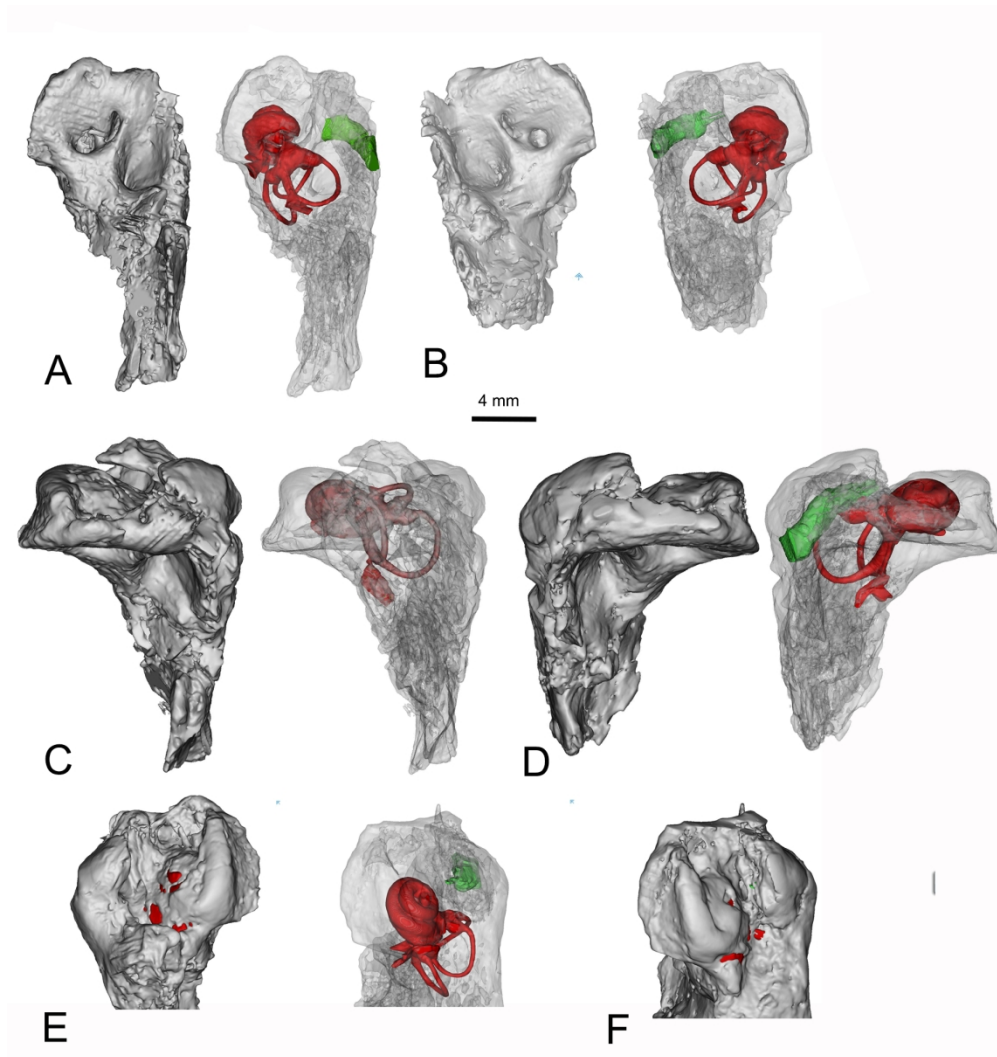


Fig. 6. 3D digital model of the petrosals of *Ocepeia daouiensis*, specimen MNHN.F.PM45, with the labyrinth by transparency. (A), right petrosal in cerebellar view; (B), left petrosal in cerebellar view; (C), right petrosal in anterior view; (D), left petrosal in anterior view; (E), right petrosal in tympanic view; (F), left petrosal in tympanic view. In red the labyrinth, in green the canal for the ramus superior (of the stapedia artery) within the tegmen tympani. Scale-bar: 4mm

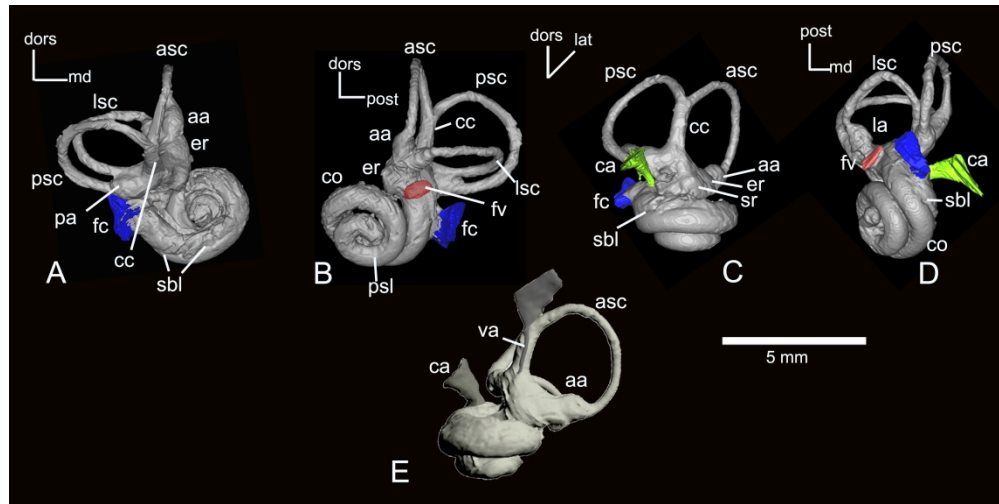


Fig. 7. 3D reconstructed digital model of the left bony labyrinth of *Ocepeia daouiensis*, specimen MNHN.F.PM45. (A) dorsal view, (B) anterior view, (C) medial view, (D) ventral view and (E) medio-anterior view. Abbreviations: aa anterior ampulla, asc anterior semicircular canal, av aquaeductus vestibuli, cc crus commune, cca cochlear canaliculus, co cochlea, er elliptical recess, fc fenestra cochleae, fv fenestra vestibuli, la lateral ampulla, lsc lateral semicircular canal, pa posterior ampulla, psc posterior semicircular canal, sbl, secondary bony lamina, sr, spherical recess, va, vestibular aqueduct. Orientation axes: dors dorsal; md medial, lat lateral, post posterior.

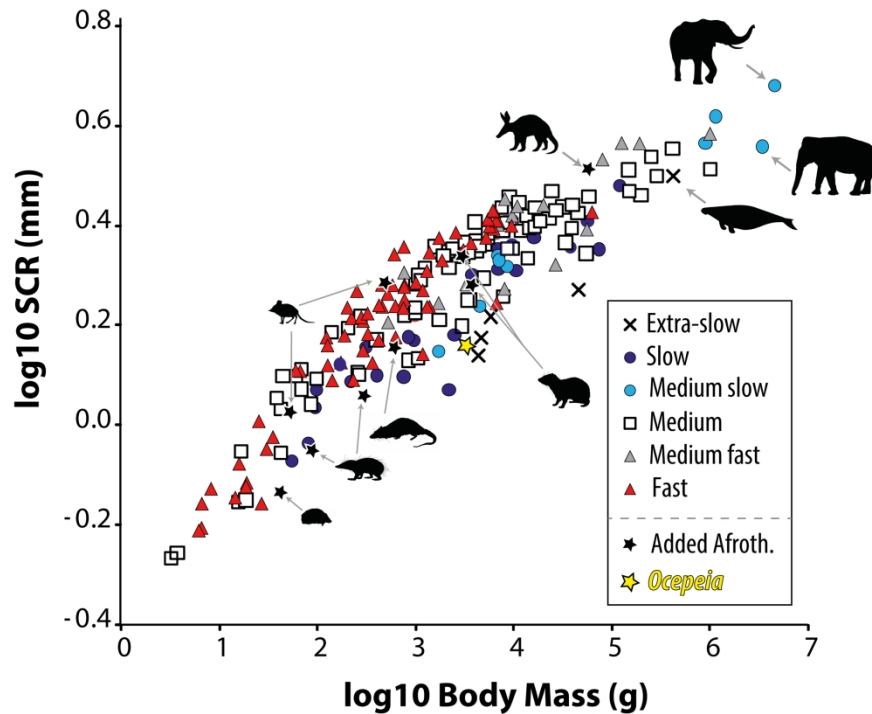


Fig. 8. Graphical relationship between the size of the semicircular canals (SCR, radius of curvature) versus body-mass (BM), with the indication of agility estimates in various mammals as measured and compiled by Spoor et al. (2007). Measurements for *Ocepeia dauiensis*, and several extant afrotherians such *Orycteropus*, *Macroscelides*, *Rhynchocyon*, *Procavia*, *Dendrohyrax*, *Potamogale*, *Tenrec*, *Tenrec*, *Chrysochloris*, *Hemicentetes* were added to the dataset (silhouettes from PhyloPic website) (see SuppData S3). This diagram shows that *Ocepeia* and the insectivore-like afrotherians (Tenrecoidea) are characterized by a relative small size of the semicircular canals with respect to other mammals of the same body mass.

Measurements and Ratios (mm)	<i>Mimoperadectes houdei</i> USNM 482355	morphotype VIII Itaborai Metatheria MNRJ 6735-V (with PET H estimated from other specimens)	morphotype euth. I Tiupampa MHNC uncatalogued	morphotype euth. II Tiupampa MHNC uncatalogued
PET L	4.41	1.34	7.23	5.08
PET W	6.23	1.43	5.93	4.40
PET H	6.66	2.67	9.67	6.65
(PET L + W + H) / 3 = PET size	5.77	1.81	7.61	5.38
IEH	4.23	2.32	5.15	3.51
log PET size	0.76	0.26	0.88	0.73
log IEH	0.63	0.37	0.71	0.55

Billet et al 2015 Billet et al 2015 Billet et al 2015 Billet et al 2015

Ocepeia	
log IEH	0.755
log PIMS	0.987

<i>Tamandua tetradactyla</i> UMCZ E581	<i>Choloepus didactylus</i> UMCZ E81	<i>Megatherium</i> sp. MNHN-F- TAR 1291	<i>Alcidorbignya inopinata</i> MHNC 8360	<i>Baiococonodon nordicum</i> YPM- PU 14234	<i>Didelphodus altidens</i> USNM 18369
8.11	10.71	51.50	5.25	5.55	5.22
11.89	11.15	45.10	5.96	5.67	4.64
14.76	13.51	54.40	7.80	7.98	6.29
11.59	11.79	50.33	6.34	6.40	5.38
9.06	8.52	20.37	4.33	4.71	3.77
1.06	1.07	1.70	0.80	0.81	0.73
0.96	0.93	1.31	0.64	0.67	0.58
Billet et al 2015	Billet et al 2015	Billet et al 2015	Billet et al 2015	Billet et al 2015	Billet et al 2015

For Peer Review Only

<i>Deltatherium</i> sp. AMNH 16610	<i>Procavia</i> <i>capensis</i> STIPB M6605	<i>Astrapotherium</i> sp. MNHN-F-SCZ 8	Notoungulata MNHN-F-BRD 23	Notoungulata UFRJ-DG 1039M	Elephantimorph 1 TMM 933-950
9.10	9.93	20.84	7.03	8.51	40.00
9.20	7.98	23.19	6.16	8.95	51.25
11.72	9.94	42.71	7.31	9.81	56.25
10.01	9.28	28.91	6.83	9.09	49.17
5.67	8.08	13.27	5.26	6.15	19.00
1.00	0.97	1.46	0.83	0.96	1.69
0.75	0.91	1.12	0.72	0.79	1.28
Billet et al 2015	Billet et al 2015	Billet et al 2015	Billet et al 2015	Billet et al 2015	Billet et al 2015

For Peer Review Only

Panameriungula te? GROUP 2 UFRJ-DG 124M	Panameriungula te? GROUP 2 UFRJ-DG 1046M	Panameriungula te? GROUP 3 UFRJ-DG 1045M	Panameriungula te? GROUP 3 UFRJ-DG 125M	Panameriungula te? GROUP 4 RHcoll uncatalogued	Ocepeia
9.73	8.67	12.49	14.95	8.22	8.91
10.22	6.39	10.03	12.42	9.07	6.29
14.73	10.73	15.50	15.49	10.72	10.13
11.56	8.60	12.67	14.29	9.34	8.44
6.44	5.62	7.09	6.37	6.06	5.65
1.06	0.93	1.10	1.15	0.97	0.93
0.81	0.75	0.85	0.80	0.78	0.75

Billet et al 2015 Billet et al 2015 Billet et al 2015 Billet et al 2015 Billet et al 2015

For Peer Review Only

Phosphatherium	Eritherium
11.88	5.53
9.88	6.89
10.91	8.92
10.89	7.11
7	5
1.04	0.85
0.85	0.70

IEH estimated for
Eritherium and
Phosphatherium
(petrosal damaged)

